



Eidgenössische Technische Hochschule Zürich  
Swiss Federal Institute of Technology Zurich

# Characterization of Human iPSC-Derived Sensory Neuron Morphology on HD-MEAs

Bachelor Thesis

Martin Stüger

August 31, 2024

Advisors: Dr. Manuel Schröter, Prof. Dr. Johannes Lengler

Department of Computer Science, ETH Zürich

## Abstract

This thesis presents the development and evaluation of an automated pipeline for the extraction and analysis of the extracellular axonal action potential landscape ("neuronal footprints") of single neurons recorded on high-density microelectrode arrays (HD-MEA). The analysis thereby focuses on human-induced pluripotent stem cell (hiPSC)-derived sensory neurons. The pipeline successfully derived neuronal morphological features from spike-sorted HD-MEA data of single neurons, and enabled a comparison against ground truth imaging data obtained by confocal microscopy. The extracted neuronal skeletons demonstrate good correspondence with the known morphologies of sensory neurons, including multipolar, unipolar, bipolar, and pseudounipolar types. Further analysis of pseudounipolar neurons allowed for the classification of axonal branches into peripheral and central axons based on conduction velocity. Notably, the conduction velocities along neuronal processes measured in this study correlate well with previously reported values for the same neuronal types, further validating the accuracy of the pipeline's outputs. The thesis also introduces an automated method to select optimal electrode configurations for stimulation purposes, providing a foundation for further automation in neuronal footprint analysis. The results indicate that the pipeline is capable of producing reliable morphological data, which could be beneficial in future studies for the characterization of sensory neuron physiology and in vitro disease modelling. The work contributes to ongoing efforts in the field to improve the accuracy and efficiency of neural data analysis, while recognizing that the quality of the outputs heavily depends on the spike-sorted input data.

---

# Contents

---

<b>Contents</b>	<b>ii</b>
<b>1 Terminology</b>	<b>1</b>
<b>2 Introduction</b>	<b>3</b>
<b>3 Results and Discussion</b>	<b>5</b>
3.1 Validation and Refinement of Neuronal Skeletons from HD-MEA Recordings . . . . .	5
3.2 Comparison of Extracted Neuronal Skeletons to Confocal Microscopy Ground Truth Data . . . . .	6
3.3 Quantitative Analysis of Axonal Conduction Velocity and Latency . . . . .	12
3.4 Morphological Classification of Sensory Neurons and Differentiation of Central and Peripheral Processes in Pseudounipolar Sensory Neurons Using Conduction Velocity Metrics . . . . .	14
3.5 Correlation of Electrical Footprint and Extracted Neuronal Skeleton: Implications for Morphological and Functional Analysis . . . . .	18
3.6 Leveraging Extracted Neuronal Skeletons for Automated Computation of Recording/Stimulation Configurations Compatible with the MaxLab Live Software . . . . .	21
<b>4 Materials and Methods</b>	<b>22</b>
4.1 Cell Culture . . . . .	22
4.2 High-Density Microelectrode Array Recordings and Data Pre-processing . . . . .	22
4.3 Microscope Images and Cell Coloring . . . . .	22
4.4 Neuronal Conduction Velocity Estimation . . . . .	23
4.4.1 Path Segment Velocity Computation . . . . .	23
4.4.2 Total Path Average Velocity Computation . . . . .	23
4.4.3 Path Latency Computation . . . . .	23
4.5 Pipeline for Neuronal Analysis . . . . .	24
4.5.1 Module 1: Visualization of Neuronal Activity Dynamics Using 3D Matrix Data and GIF Creation . . . . .	24
4.5.2 Module 2: Neuronal Footprint Skeletonization and Post-Processing for Accurate Path Reconstruction . . . . .	25
4.5.3 Module 3: Axon Classification and Output Visualization Following Post-Processing . . . . .	27
4.5.4 Module 4: Inferring HD-MEA Electrode Configurations for Targeted Neuronal Stimulation . . . . .	30

4.5.5	Module 5: Amplitude Waveform Visualization of Neuronal Activity Along Reconstructed Paths . . . . .	31
<b>5</b>	<b>Outlook</b>	<b>33</b>
	<b>Bibliography</b>	<b>34</b>

## Chapter 1

---

# Terminology

---

In this section, we introduce key terminology that will be essential for an understanding of the presented methodologies and results of this thesis.

**Electrical Footprint:** The spatio-temporal representation of spike sorted neural electric activity of a single neuron recorded by a high-density microelectrode array (HD-MEA); an electrical footprint consists mainly of the recorded axonal action potential signal.

**Skeletonization:** An analysis process that identifies the main neuronal compartments from an electrical footprint.

**Neuronal Skeleton:** A simplified representation of a neuron's structure, extracted through the skeletonization process (mainly the axon).

**Initiation Site:** The point of a neuronal electrical footprint corresponding to the first electrode with a signal amplitude significant enough to be included in the neuronal skeleton.

**Extracellular Action Potential:** The electrical signal detected outside a neuron, representing the difference in voltage across the cell membrane as an action potential passes.

**Trough Amplitude:** The magnitude of the negative peak in an extracellular action potential waveform.

**Spike Sorting:** A computational process used to separate individual neuronal signals from the inter-mixed signals recorded by HD-MEAs.

**Active Sensing Area (ASA):** The area of an HD-MEA where the micro-electrodes are located and where extracellular signals can be recorded.

**High-Density Microelectrode Arrays (HD-MEAs):** Devices that contain a densely packed array of micro-electrodes. These electrodes can be used to record extracellular electrical activity from neurons and other electrogenic cells. The current study used plates composed of multiple HD-MEAs.

**Electrode Configuration:** The specific arrangement of 1020 electrodes on an HD-MEA used to record or stimulate neuronal activity.

**Neuronal processes:** The extensions/compartments of a neuron, including axons and dendrites, that transmit electrical signals and connect the neuron to other cells.

**Crosstalk:** The unintended overlap or interference between signals recorded by adjacent electrodes on an HD-MEA.

**tdTomato:** A fluorescent protein used as a marker in biological imaging which emits a bright red/orange fluorescence when exposed to specific wavelengths of light.

**Electrode Configuration:** The specific arrangement of electrodes on an HD-MEA used to record and stimulate neuronal activity.

## Chapter 2

---

# Introduction

---

The analysis of the morphology of sensory neurons derived from human-induced pluripotent (hiPSC) stem cells is crucial for advancing our understanding of their functions. Studies have shown that human sensory neurons, which can be generated *in vitro* using specific protocols [1], can effectively model human peripheral sensory neurons, making them crucial for investigating conditions such as chronic pain and itch [2], [3]. It is possible to functionally characterize the generated sensory neurons using high-density microelectrode arrays (HD-MEAs), which offer the capability to record neural activity at high spatial and temporal precision [4], [5]. However, the extraction of meaningful morphological data from HD-MEA recordings presents significant challenges due to the complexity and volume of the data. Recent studies have sought to overcome these challenges by developing automated methods for axon reconstruction [6], [7] and advanced approaches for electrophysiological phenotyping [8], which have enhanced our understanding of neuronal morphology and function in both healthy and diseased states. This thesis focuses on the development of an automated pipeline for extracting neuronal skeletons from spike sorted single-unit HD-MEA recordings. The primary aim of this thesis is to improve the accuracy of neuronal skeleton extraction, which involves isolating the morphological features of neurons. The quality of the extracted neuronal skeletons is assessed by comparing them against ground truth data obtained from confocal microscope images. This comparison not only validates the skeletonization process, but also facilitates the classification of neural compartments.

A recent study by Chelsey J. LeBlang et al. [1], which used a similar coculture of rodent Dorsal Root Ganglion satellite glia cells and human-induced sensory neurons, identified four distinct sensory neuron morphologies: multipolar, unipolar, bipolar, and pseudounipolar (Figure 2.1). Examples of these morphological types were also observed in the dataset of the extracted neuronal skeletons and are presented in this thesis. The many different morphologies highlight the challenges involved in classifying sensory neuron morphology *in vitro*.

Neurons with pseudounipolar morphology are of particular interest, as they are the first neurons of the sensory pathway in adult humans [10]. They have a distinctive T-shaped structure, where a stem axon emerges from the soma and then bifurcates into a central axon and a peripheral axon [11]. To better analyze these neurons, we developed a more accurate method, as part of the presented neuron analysis pipeline (section 4.5). Classifying the axons of pseudounipolar sensory neurons as either peripheral axon or central axon based on differences in their conduction velocity observed in past studies [12].

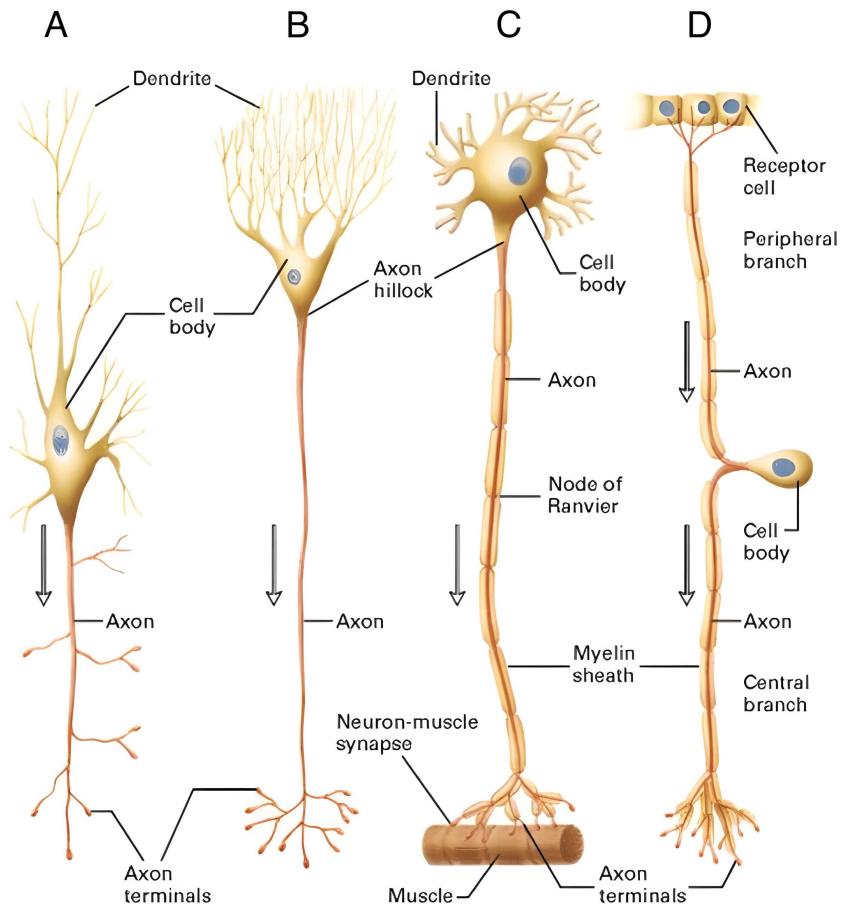


**Figure 2.1:** Types of sensory neuron morphologies with the main compartments labeled and the signal propagation direction in the axons indicated by an arrow. (A) Bipolar, (B) Unipolar, (C) Multipolar, (D) Pseudounipolar ([9])

Additionally, the thesis introduces an automated method for selecting optimal electrodes for HD-MEA recording configurations, which can be used within the MaxLab Live software by MaxWell Biosystems, a platform designed for the real-time control and monitoring of HD-MEAs [13]. The pipeline also generates outputs that allow for a manual analysis of the electrical footprint of neurons, a task that I aim to automate in the future.

The advancements in the skeletonization processes presented in this thesis are intended to support further research efforts by providing a reliable and automated method for analyzing the morphology and functionality of these and other neurons.

## Chapter 3

---

# Results and Discussion

---

In this section, we present our analyses and findings, focusing on the extraction and validation of neuronal skeletons obtained from high-density microelectrode array (HD-MEA) axon tracking recordings. We first evaluate the accuracy of the axon skeletonization process, by comparing primary neuronal processes inferred from electrical footprints, to confocal microscope images. Further, we derive metrics such as axon conduction velocity and latency, computed during the skeletonization process, and compare them with previously reported values. A detailed explanation on how the velocity and latency were computed is provided in section 4.4. Next, we correlate these metrics with structural properties of neurons. Specifically, we perform a detailed morphological analysis of neurons with putative pseudounipolar morphology. In addition, we manually analyze the electrical footprint of a neuron, identifying its potential neuronal compartments by examining electrophysiological properties and conducting an analysis of the waveform features. While this analysis is done manually, it demonstrates the potential for significant improvements in the accuracy of skeletonization and neuronal compartment classification if automated and incorporated into the pipeline.

### 3.1 Validation and Refinement of Neuronal Skeletons from HD-MEA Recordings

For the following analyses, we considered a total number of 177 input GIFs, respectively putative electrical footprints, from one HD-MEA recording (for more information on the recording refer to section 4.2). Of these 177 units, 155 passed the noise threshold and were considered for the skeletonization (for details on this analysis, see section 4.5.2). To assess the accuracy and quality of the skeletonization process, we manually compared the extracted neuronal skeletons with the corresponding input GIFs by tracking how the skeleton extended in each frame of the GIFs. This manual evaluation was necessary because, as of today, no automated method is available to probe the quality of the extracted skeletons with non-simulated data [6]. We also used confocal microscope images as ground truths to verify the accuracy of the extracted neuronal skeletons, which will be further discussed in section 3.2. The final neuronal skeleton was generated following several additional post-processing steps, as detailed in section 4.5.2. These steps involved discarding extraneous paths within the neuronal skeleton, which may result from noise, imprecise tracking, or signals lingering excessively at one location. As shown in the initial skeleton (Figure 3.1A), very short branches emerging from longer paths were removed in the post-processed skeleton (Figure 3.1B). The example in Figure 3.1 also demonstrates that the skeletonization process, can

handle overlapping neural processes. It is important to note that in the plots of the neuronal skeleton, each path starts at the initiation site marked with a red dot. This means that the paths share all centroids up to their split point. If one analyzes the extracted footprint by the MaxLab Live Software [13] (Figure 3.1C) it is visible that there are some sections with a very weak signal or a complete signal interruption. This is likely caused by other neurons or cells, such as glia cells, that were co-cultured with the sensory neurons on the HD-MEA, and thus may have weakened the measured amplitude at least at some locations on the chip/footprint. However, we found that the developed program was robust to signal interruptions like these, as is seen in the the extracted neuronal skeletons in Figure 3.1.

### 3.2 Comparison of Extracted Neuronal Skeletons to Confocal Microscopy Ground Truth Data

Next, we compared the extracted skeletons of neurons to confocal images that were taken after the HD-MEA recordings. A direct alignment was possible, because the sensory neurons used in this study expressed dtTomato. Of the eight ground truth units, that we found for these recordings, three were sufficiently visible on the microscope images, with exactly one ground truth for each of the three wells (1, 4, and 5). However, for all three ground truth data sets, the neuronal somas were located outside the active sensing area. Despite that limitation, we were still able to locate the axonal processes beyond the edge of the active sensing area. It is noteworthy, that almost all somata on these microscope images were not located on the active sensing area as can be seen in Figure 3.2 of well 1 in which the somata are mostly below the bottom edge of the active sensing area. A technique to prevent neurons moving away from the chip would be beneficial for future work. The ground truth also allowed for the morphological classification of neurons and further quality assessment of various metrics, beyond just the extracted neuronal skeleton quality. These metrics are described in section 3.3.

The first ground truth found on well 1 is displayed in Figure 3.3. In the extracted neuronal skeleton, axon 2 clearly follows the same course as a visible process of a bipolar, bell-shaped neuron in the microscope image. A bipolar neuron is described as bell-shaped, if it is undergoing the transformation from a bipolar to a pseudounipolar morphology, where the angle between its two processes is less than 90 degrees [10]. The other process of this neuron, which comprises axons 1 and 3, shows a clear course change to the right at the initiation site marked with a red dot on the neuronal skeleton. This course change, labeled as the 'Right curve of Axon 1,3' in Figure 3.3B, is visible in both the neuronal skeleton and the microscope image. The bifurcation of this process into axons 1 and 3 is also visible in the microscope image, though not as distinctly as the other features.

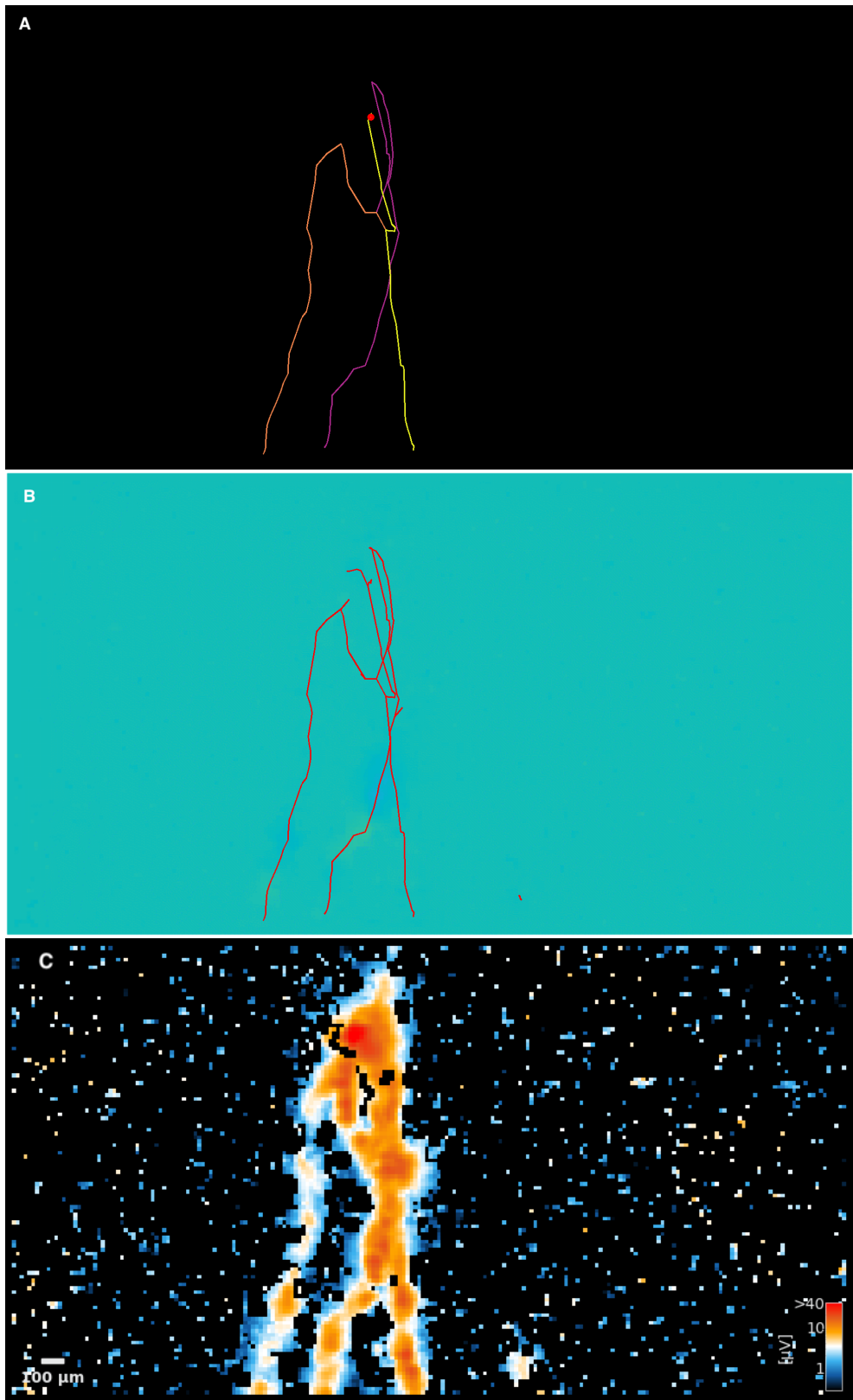


**Figure 3.1:** Comparative analysis of neuronal skeleton extraction and refinement for unit 11 on well 5. (A) Refined final neuronal skeleton after post-processing steps, with a red circle indicating the initiation site. Different paths are colored for easier identification. (B) Overlay of the last frame from the input GIF with the initially extracted skeleton. (C) Footprint generated by the MaxLab Live Software [13], showing the spatial distribution of recorded amplitudes in the neuron.

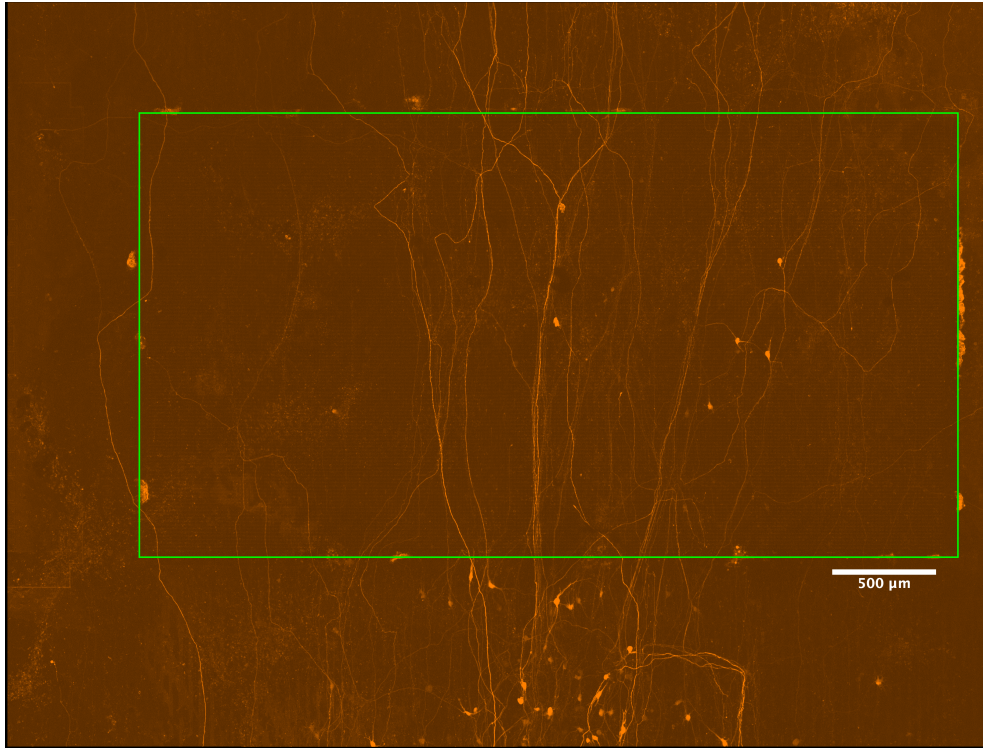


**Figure 3.2:** Microscope image of well 1. The Active Sensing Area (ASA) ( $3.85 \times 2.10 \text{ mm}^2$ ) is outlined in light green. Most somas are located outside the active sensing area.

The second ground truth found on well 4 is displayed in Figure 3.4. Both primary axons, 1 and 3, are clearly visible in the microscope image. Axon 2 in the neuronal skeleton can be disregarded, as it is too short to allow for a proper comparison. Additionally, there is an unidentified process originating from the same neuron's soma, but its signal was too weak and too distant from the other processes detected to be considered part of the skeleton by the gifskeletonization.py program. Without this unidentified process, the neuron could be classified as pseudounipolar. However, the presence of this third processes signal at the very end of the input GIF strongly indicates a multipolar morphology, with axons 1 and 3 forming a pseudounipolar-like stem structure. It is also important to note a slight error in the neuronal skeleton, where axon 1 makes an unexpected sharp left turn at the top edge of the active sensing area in the neuronal skeleton, which is not visible in the microscope image.

The third ground truth found on well 5 is displayed in Figure 3.5. Both axons, 1 and 2, are clearly visible in the microscope image. This neuronal skeleton demonstrates the potential accuracy that the gifskeletonization.py program can achieve. All the turns and the split visible in the microscope image, are captured in the neuronal skeleton. Although the soma of this

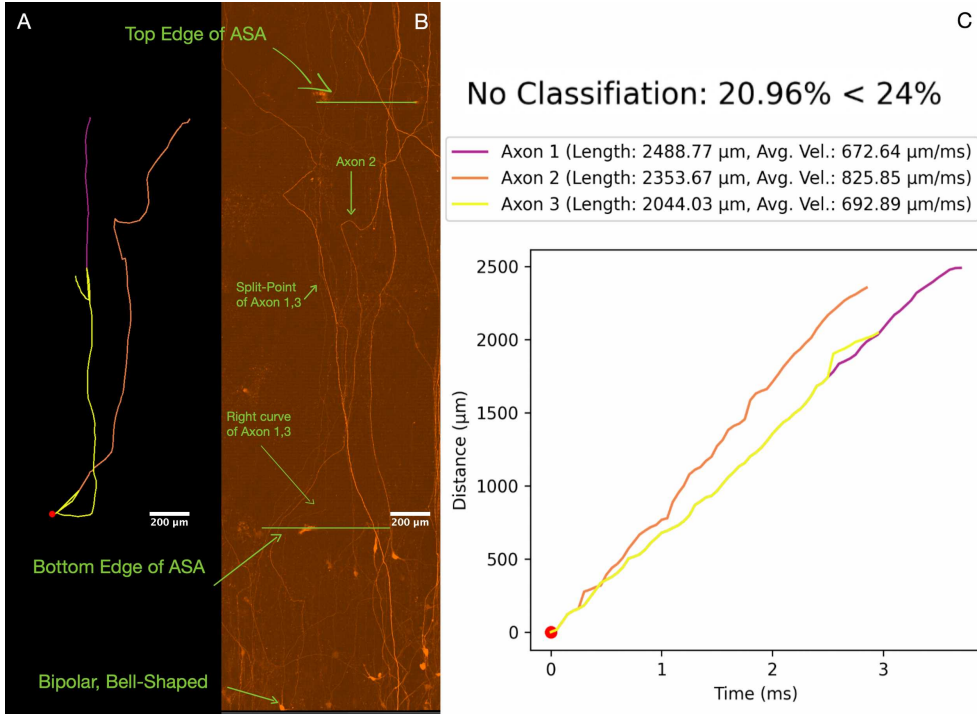


**Figure 3.3:** (A) Final neuronal skeleton of neuron unit 22 on well 1. (B) Cropped microscope image of well 1 with labeling to identify the edges of the active sensing area (ASA) and facilitate location of the relevant processes and soma. (C) Maximum average conduction velocity difference found between two processes in the neuronal skeleton. A difference of 20.96% is insufficient for classifying the neuron's processes. Also shown are the total length, average conduction velocity, and conduction velocity plots for each tracked process.

neuron is harder to discern in the microscope image, it is evident that the neuron is multipolar, as more than three processes extend from its soma. One process that enters the active sensing area and several branches off axon 1 are not displayed in the neuronal skeleton. There was no indication of these processes in any frame of the input GIF. Therefore, the issue lies not with the gifskeletonization.py program's tracking, but rather within the spike sorting step.

These three ground truths demonstrate that the skeletonization process of the gifskeletonization.py program is capable of producing very accurate results, although the accuracy of outcomes is heavily dependent on the quality of the input GIFs.

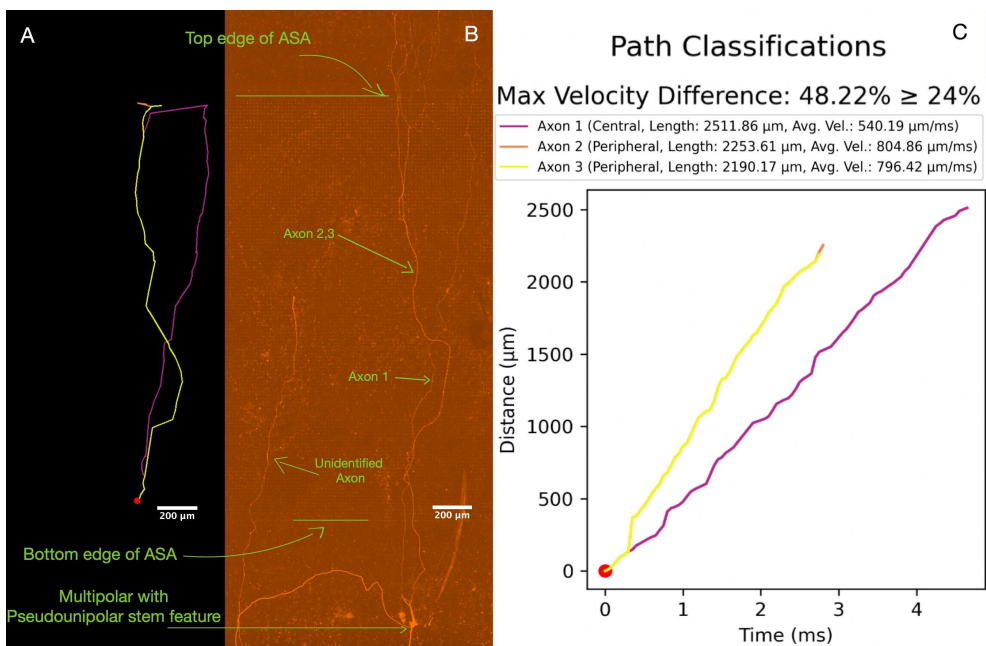


**Figure 3.4:** (A) Final neuronal skeleton of neuron unit 28 on well 4. (B) Cropped microscope image of well 4 with labeling to identify the edges of the active sensing area (ASA) and facilitate location of the relevant processes and soma. (C) Maximum average conduction velocity difference found between two processes in the neuronal skeleton. A difference of 48.22% is sufficient for classifying the neuron's processes. Also shown are the classification, total length, average conduction velocity, and conduction velocity plots for each tracked process.

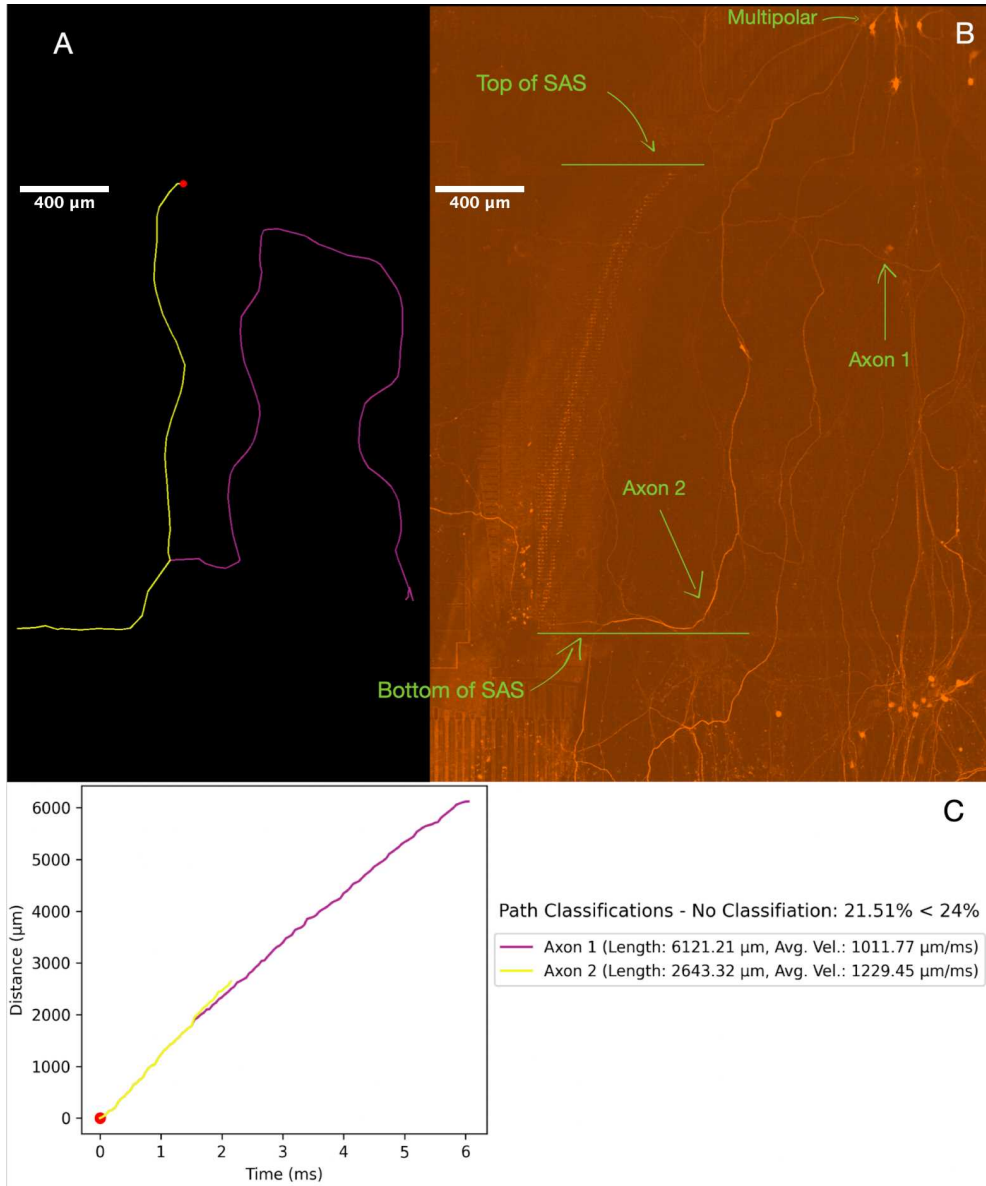


**Figure 3.5:** (A) Final neuronal skeleton of neuron unit 52 on well 5. (B) Cropped microscope image of well 5 with labeling to identify the edges of the ASA and facilitate location of the relevant processes and soma. (C) Maximum average conduction velocity difference found between two processes in the neuronal skeleton. A difference of 21.51% is insufficient for classifying the neuron's processes. Also shown are the total length, average conduction velocity, and conduction velocity plots for each tracked process.

### **3.3 Quantitative Analysis of Axonal Conduction Velocity and Latency**

Several metrics were calculated as part of the skeletonization process: The conduction velocity and latency from the initiation site along each neuronal process, as well as the average conduction velocity across all neuronal processes within each neuron, were computed prior to morphological classification and are displayed in Figures 3.6, 3.11. Several reports have categorized primary sensory neurons based on their conduction velocity into C-cells, A $\delta$ -cells and A $\alpha/\beta$ -cells [14], [12], [15]. Since the human pluripotent stem cells on the HD-MEA plate were not cultured under conditions to form myelinated axons, the computed average velocity was expected to fall within the range of unmyelinated C-fibre cells [1]. The conduction velocity of C-fibre cells in rats were found to be slower than 1.4 m/s [12], [14]. This is consistent with the average conduction velocity range computed in the 155 analyzed neurons, which was between 424.28  $\mu\text{m}/\text{ms}$  and 1211.11  $\mu\text{m}/\text{ms}$  (Figure 3.11). The fastest conduction velocity computed for a single process was 1467.6  $\mu\text{m}/\text{ms}$  (Figure 3.11). Considering that the velocity range for A $\delta$ -fibre cells (the second slowest fibre group) lies between 2.2 m/s and 8 m/s [14], the facts that the fastest process was only 0.0676 m/s above the C-fibre classification limit, and that this was the only computed velocity above 1.4 m/s, does not invalidate the program's accuracy in tracking velocities along the processes of a neuron. In all ground truth data sets, such as displayed in Figures 3.3, 3.4, 3.5, it is visible that the processes which appear to have a larger diameter in the microscope images also have higher average velocities. Larger diameter axons tend to have higher conduction velocities because the increased diameter reduces the internal resistance to the flow of electrical current within the axon [16], [17]. This correlation between diameter and conduction velocity further validates the accuracy of our velocity computation, as it aligned with established biophysical principles.

The latency, i.e., the time delay of the signal from its initiation site as it travels along the neuron's processes, was mainly used to help users see in which direction the signal travels along the processes, as inferring the signal flow can be difficult if one has not seen the input GIF and/or the neuron has overlapping processes. For example, in Figure 3.1, it may be challenging for the user to determine in which direction the signal travels through the process colored in pink. However, the latency plot in Figure 3.7 makes it easy to identify the direction of signal travel along this process, with red indicating shorter delays and blue indicating longer delays.

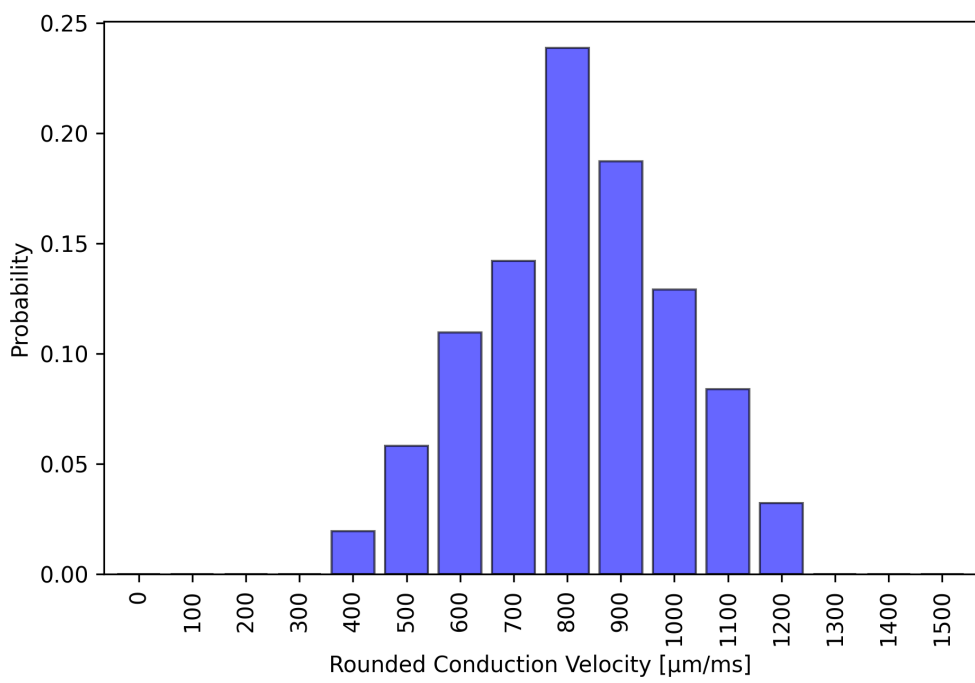


**Figure 3.6:** Probability density function graph of average velocity values computed for each neuron, rounded to the nearest 100  $\mu\text{m}/\text{s}$ .

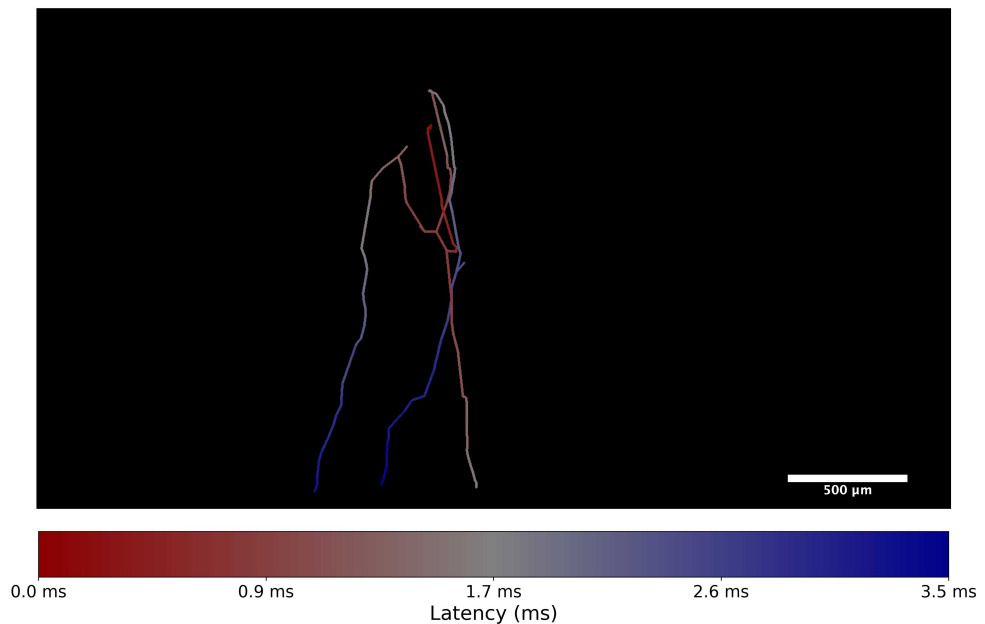
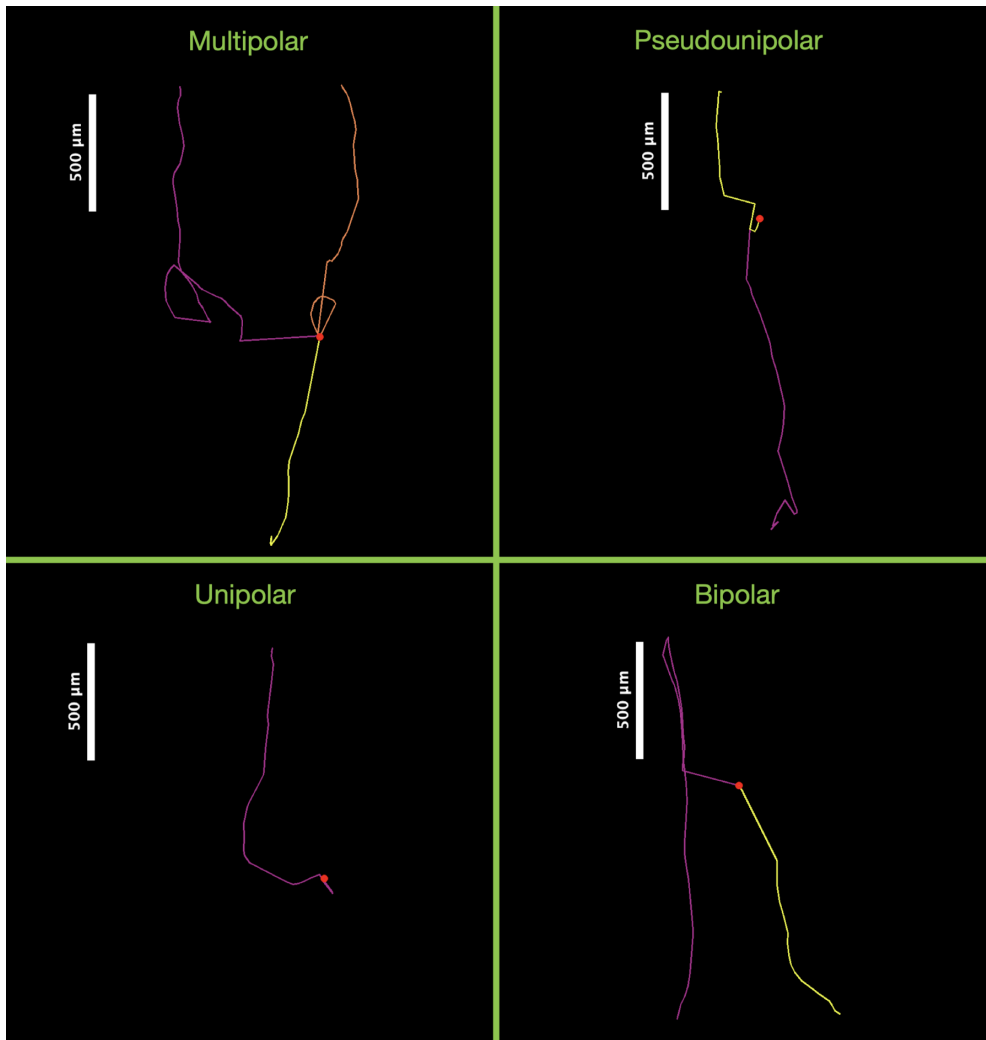


**Figure 3.7:** Latency plot for neuron unit 11 on well 5, with values ranging from 0.0 ms in dark red to 3.5 ms in dark blue.

### **3.4 Morphological Classification of Sensory Neurons and Differentiation of Central and Peripheral Processes in Pseudounipolar Sensory Neurons Using Conduction Velocity Metrics**

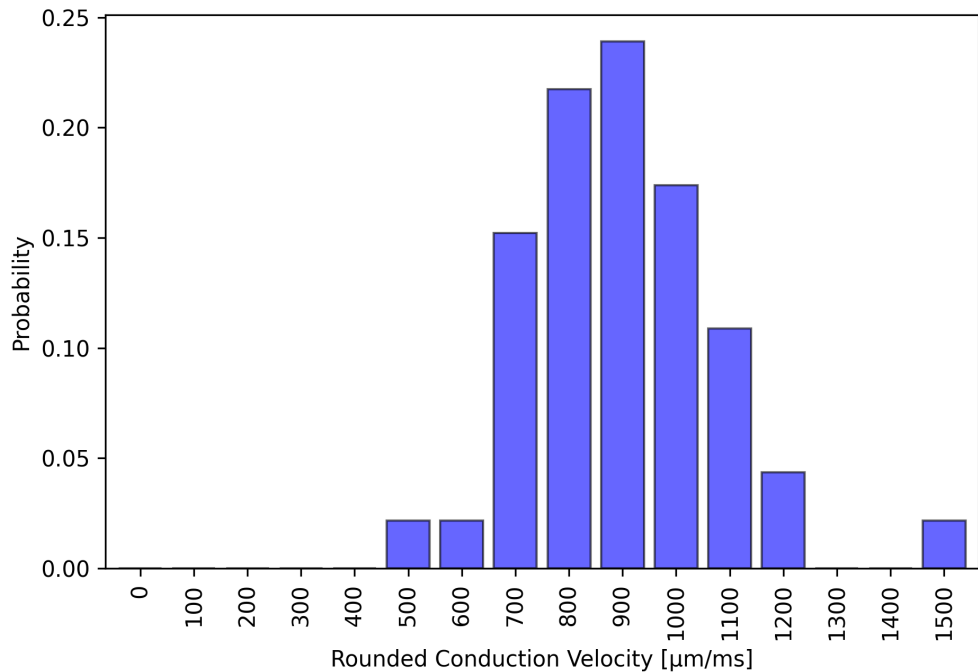
To accurately perform morphological classifications, it is essential to understand the four different morphological categories exhibited by the sensory neurons. Human iPSC-derived sensory neurons were co-cultured with rat dorsal root ganglion (DRG) cells to facilitate morphological transformation from an initial bipolar to a pseudounipolar morphology [1] (details on cell culture in section 4.1). In addition to bipolar and pseudounipolar morphologies, sensory neurons cultured *in vitro* may also adopt unipolar or multipolar morphologies. Previous studies on iPSC-derived sensory neurons co-cultured with rat DRG cells have looked into the morphological distribution and revealed the following proportions: 46% multipolar, 9% unipolar, 7% bipolar, and 38% pseudounipolar [1]. Neuronal skeleton examples for each morphological class as found in our data are displayed in Figure 3.8. The multipolar and unipolar morphology can be identified based on the number of processes emerging from the soma. Unipolar neurons have one process, while multipolar neurons have more than two [11]. If a neuronal skeleton shows two processes, it is classified as either pseudounipolar or bipolar. A bipolar neuron is characterized by two processes extending from the soma in opposite directions [11]. In contrast, a pseudounipolar neuron has a stem process extending from the soma, which bifurcates into a peripheral and a central process, forming a distinctive T-shape that facilitates its identification [10], [18], [19]. The four morphological examples displayed in Figure 3.8 were selected based on the assumption that the location of the first detected signal corresponds to the soma of the respective neuron and that signal propagation in a process can occur bidirectionally *in vitro*. This bidirectional axonal conduction behavior has been observed to occur frequently in DRG neuronal cell cultures [20].

Next, we performed a more detailed analysis of the neuronal skeletons with a putative pseudounipolar morphology. Neuronal skeletons with only one process were discarded, resulting in 119 neuronal skeletons being considered. Specifically, the aim was to accurately detect and label the peripheral and central processes of neurons with a pseudounipolar morphology. Peripheral processes have been reported to have a higher conduction velocity than central processes [12], [21]. This was the primary criterion for classifying the processes in the neuronal skeletons. Of the 119 multi-branched input skeletons, 46 classifications were made (Table A in Figure 3.11) by identifying the split point with the highest average velocity difference between two processes in each neuronal skeleton (referred to as the maximum split point). If the average velocity difference of the processes that split at the maximum

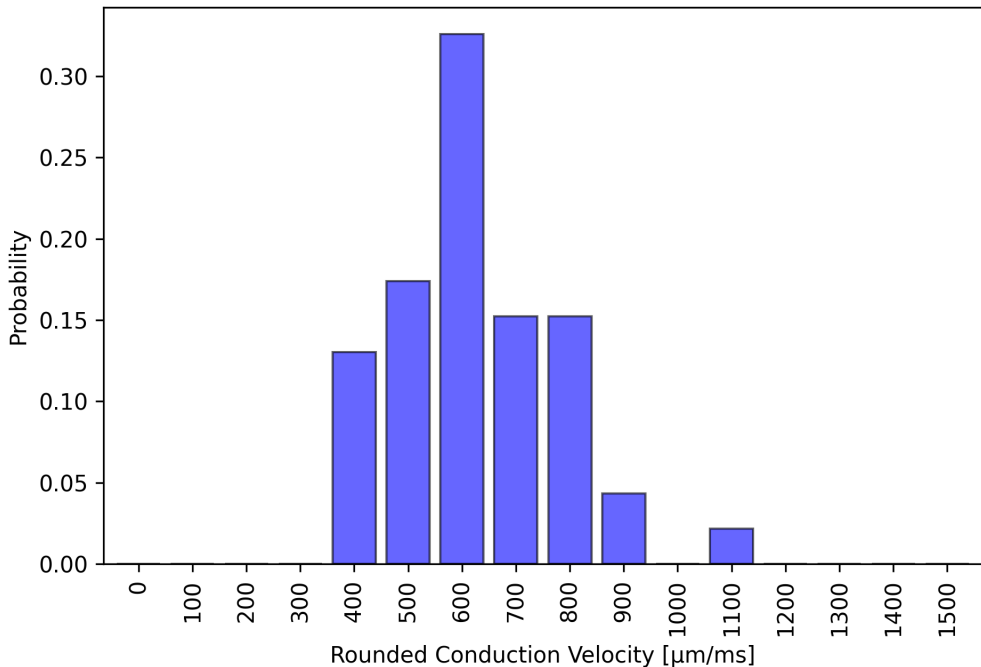


**Figure 3.8:** Extracted neuronal skeletons of each primary sensory neuron morphology type found in the co-culture of iSNs and rSGs.

split point was higher or equal to 24%, the slower process was labeled as central and the faster process was labeled as peripheral. If the highest average velocity difference across all split-points in a neuronal skeleton was less than 24%, no classification was made. The average velocity difference between the peripheral and central processes in pseudounipolar C-fibre cells has been reported to be 28% in rats [12] and 18% in cats [21]. The threshold of 24% was selected as it provides an intermediate value between the observed species-specific velocity differences, ensuring a classification criterion that is appropriately sensitive to variations while also minimizing the risk of false positives. The conduction velocity computed for the peripheral processes ranged from 488.5  $\mu\text{m}/\text{ms}$  to 1467.6  $\mu\text{m}/\text{ms}$ , with the value of 1467.6  $\mu\text{m}/\text{ms}$  being the only one exceeding 1200  $\mu\text{m}/\text{ms}$  (Figure 3.9). The conduction velocities computed for the central processes ranged from 377.17  $\mu\text{m}/\text{ms}$  to 1097.19  $\mu\text{m}/\text{ms}$  (Figure 3.10). These values are consistent with the ranges previously reported for pseudounipolar rat primary sensory neurons, which fall between 0.4 m/s and 1.3 m/s for the peripheral processes and 0.3 m/s and 1.1 m/s for the central processes [12].



**Figure 3.9:** Probability density function graph of average velocity values computed for the peripheral processes of neurons classified as pseudounipolar, rounded to the nearest 100  $\mu\text{m}/\text{s}$ .



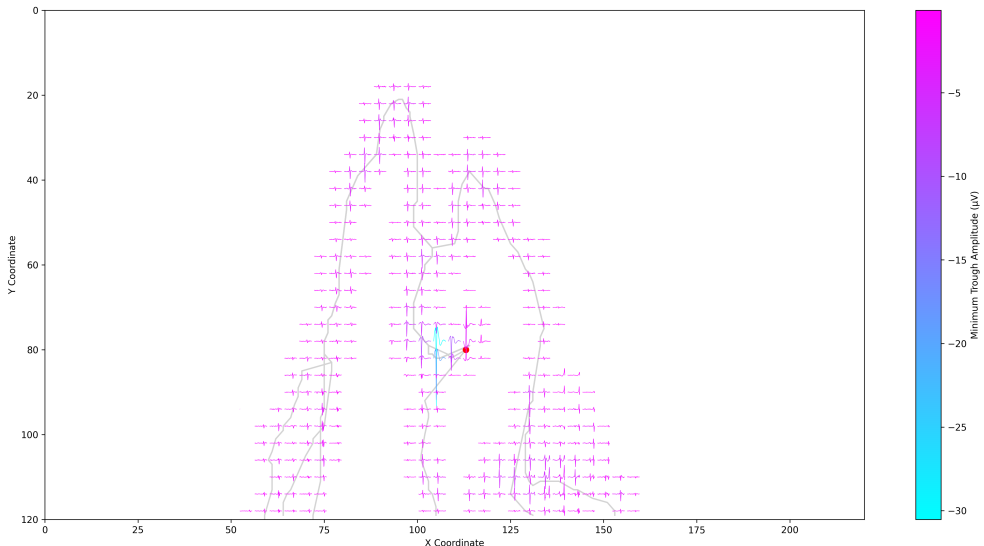
**Figure 3.10:** Probability density function graph of average velocity values computed for the central processes of neurons classified as pseudounipolar, rounded to the nearest 100  $\mu\text{m}/\text{s}$ .

Table A Metric		Count				
<b>Analyzed Neurons</b>		155				
<b>Neurons with Branches</b>		119				
<b>Classifications</b>		46				
Table B		Mean	Std	CV	Median	Min
<b>Average Neuron Velocity [μm/ms]</b>		826.59	177.87	0.22	828.61	424.28
<b>Velocity Peripheral Axon [μm/ms]</b>		889.48	180.13	0.2	864.12	488.5
<b>Velocity Central Axon [μm/ms]</b>		626.99	146.61	0.23	606.55	377.17
<b>Velocity Difference [%]</b>		44.85	28.39	0.63	34.46	24.02
<b>Longest Latency [ms]</b>		2.96	1.35	0.46	2.55	0.6
						6.25

**Figure 3.11:** Table A shows the count of: 1) Neurons that passed the noise threshold and had a neuronal skeleton extracted. 2) Neurons with more than one branch. 3) Neurons identified as pseudounipolar, for which the processes were classified as central or peripheral. Table B shows the mean, standard deviation, coefficient of variation, median, minimum, and maximum of: 1) Average neuron velocity computed across all processes in a neuron. 2) Average velocity of processes classified as peripheral. 3) Average velocity of processes classified as central. 4) Average velocity difference between the peripheral and central processes in neurons classified as pseudounipolar. 5) Longest latency from the location where the first signal was detected.

### 3.5 Correlation of Electrical Footprint and Extracted Neuronal Skeleton: Implications for Morphological and Functional Analysis

Neurons exhibit significant diversity in their electrophysiological properties, making the analysis of their electrical footprints essential for categorizing them and identifying their functional roles [22], [23]. Automating this analysis and integrating it into the analysis pipeline could significantly enhance the precision of neuron compartment identification and overall functionality assessment, as demonstrated by recent studies aimed at achieving automated phenotyping [24], which could greatly improve research throughput in future work. The electrical footprint overlaid onto the neuronal skeleton of unit 10 on well 5 is presented in Figure 3.12. Although the extracted neuronal skeleton of unit 10 showed a potential match with a neuron in the confocal microscope image of well 5, the match was not clear enough to serve as a definitive ground truth, rendering it unsuitable for demonstration it as such in this thesis. Nevertheless, the alignment of the electrical footprint with the extracted skeleton is evident, as the amplitude plots farther from the neuronal skeleton show diminished peak voltage amplitudes. Amplitude waveforms which did not exceed a negative or positive voltage of  $0.4 \mu\text{V}$  were filtered out and are not plotted.



**Figure 3.12:** Electrical footprint waveforms overlaid onto the neuronal skeleton (gray) of unit 10 on well 5 that were extracted by the analysis pipeline. Waveforms are color-coded based on their minimum trough amplitude, ranging from  $0 \mu\text{V}$  (pink) to  $-30 \mu\text{V}$  (light blue). The waveforms represent averaged signals from  $4 \times 4$  electrode blocks. To enhance image clarity, each waveform plot was scaled by a factor of 0.5. The initiation site is marked with a red dot.

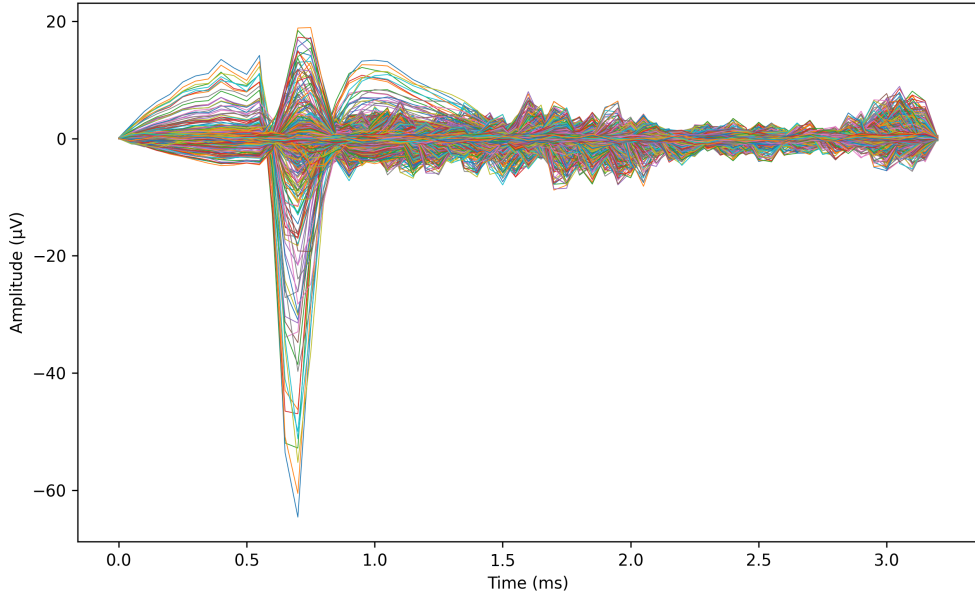


**Figure 3.13:** Spike-sorted waveforms showing neuronal activity of unit 10 on well 5 captured across multiple electrodes in the HD-MEA recordings, truncated to a length of 3.5 ms.

The initiation site of unit 10, marked with a red dot, is located centrally on the active sensing area (ASA). The waveforms at the initiation site are characterized by an initial small negative peak, followed by a large positive peak, and then another smaller negative peak. It has been reported that after an AP is generated at the distal end of the axon initial segment (AIS), the AP not only propagates into the axon(s) but also back-propagates towards the soma [25]. These back-propagated APs can produce extracellular measured amplitude waveforms with the observed pattern at the initiation site, characterized especially by a large positive peak [25]. Immediately to the left of the initiation site, the waveforms exhibit a positive peak followed by a very large negative peak, then another smaller positive peak. This waveform structure, characterized by a large and broad negative peak followed by a smaller positive peak, is typically observed near the AIS and soma [25]. The presence of the largest negative amplitudes within this area further supports the hypothesis that the AIS is located here [25]. This leaves the initial positive peak of these waveforms to be explained, which, in extracellular AP waveforms near the soma or AIS, is typically attributed to capacitive membrane currents [25]. These observations strongly indicate that the soma and AIS are located within this region. Tracing the extracted neuronal skeleton from this point reveals a bifurcation into two processes: one ascending towards the top edge of the ASA and the other descending towards the bottom edge of the ASA. It is noteworthy that an erroneous centroid was introduced in the descending process, incorrectly reconnecting it to the initiation site instead

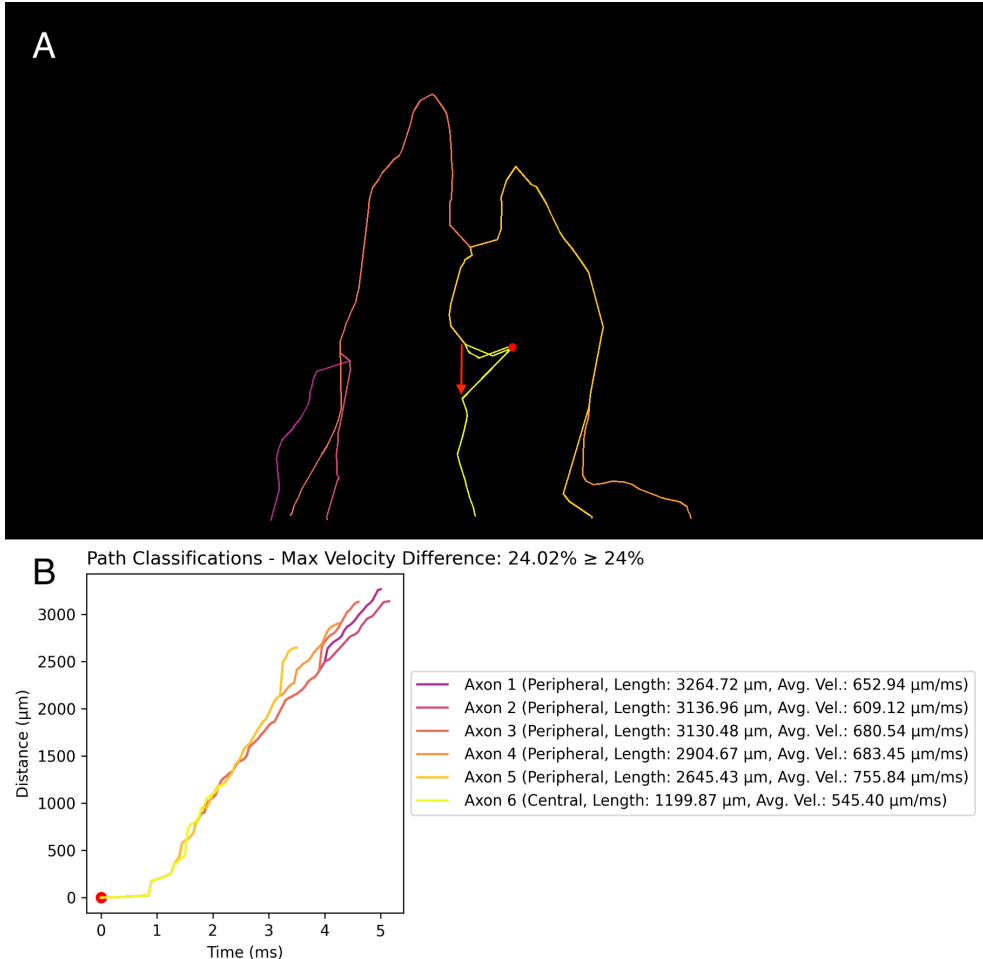


**Figure 3.14:** (A) Extracted neuronal skeleton of unit 10 on well 5. The red arrow shows a mistake, due to weakened signals, as the yellow path should be heading straight down instead of back to the initiation site and then down. (B) The computed velocity and classification for each path in the skeleton.

of continuing straight down (red arrow in Figure 3.14A). Both processes maintain a consistent bi-phasic pattern, characterized by a sharp initial positive peak followed by a sharp negative peak, a signature pattern of axonal APs [26]. Following the ascending process we can see that it bifurcates into two sub-processes which at their terminal ends again split into three (left) and two (right) processes. In these terminal processes we observe that some of the waveforms are multi-modal, which is consistent with the observation that the terminal processes are in close proximity or even cross each other, likely resulting in crosstalk among the electrodes [27]. By combining the information derived from the electrical footprint analysis of unit 10 on well 5 with the computed metrics from the analysis pipeline,

we can infer the neuron's morphology. The presence of two processes extending from the soma/AIS suggests that the neuron could be either bipolar or pseudounipolar [11]. Examination of the computed velocity metrics for this unit reveals a significant velocity difference of 24.02% (Figure 3.14B) between the two main processes, supporting the classification of the neuron as pseudounipolar [12], [21]. The descending slower process was classified as central and all the other processes were classified as being part of the peripheral process (further details on this classification can be found in section 3.4). This section demonstrates how integrating electrical footprint waveform analysis with the structural data and the computed metrics provided by the analysis pipeline can greatly enhance the reliability and accuracy of the morphological classification of neurons.

### **3.6 Leveraging Extracted Neuronal Skeletons for Automated Computation of Recording/Stimulation Configurations Compatible with the MaxLab Live Software**

After successfully extracting neuronal skeletons, we can further leverage this information for functional experimentation, specifically neuronal stimulation. The extract-electrodes.py program (explained in section 4.5.4) identifies the 1020 electrodes closest to the neuronal skeleton from the total of 26,400 electrodes. The program computes the list of electrode IDs for these 1020 electrodes, from which a configuration file (.cfg) can be generated and used for the stimulation functionality integrated in the MaxLab Live Software by MaxWell Biosystems [13]. An example of an electrode configuration for unit 22 on well 1 is shown in Figure 4.2. The stimulation process can provide valuable insights, such as determining the propagation direction of action potentials within a neuron's processes or identifying optimal locations for inducing action potentials [4], [5]. Automating the extraction of the optimal recording/stimulation configuration after the neuronal skeleton has been identified allows for highly targeted, neuron-specific recordings. While this iterative process of refining electrode recording configurations to then again enhance the skeletonization accuracy and morphological classification was not implemented or tested in this thesis, it could be a promising direction for future work.

## Chapter 4

---

# Materials and Methods

---

### 4.1 Cell Culture

In this study, we maintained human induced pluripotent stem cell (iPSC)-derived sensory neurons, in co-culture with non-neuronal cells from embryonal rat dorsal root ganglia (DRG). The iPSC-derived sensory neurons were initially cultured on high-density microelectrode array (HD-MEA) plates as a monoculture. Subsequently, to better mimic the *in vivo* neuronal environment and to induce pseudounipolar morphology, sensory neurons were co-cultured with rat DRG cells from day 3 *in vitro* (DIV3) onwards. We plated 50'000 cells and 25'000 DRG cells per HD-MEA well.

### 4.2 High-Density Microelectrode Array Recordings and Data Preprocessing

The sensory neuron co-culture was recorded a total of ten times between the 08.05.2024, and 13.06.2024. The data collected from all recordings was used to enhance the analysis pipeline. The results and data presented in this thesis are solely from the final recording on the 13.06.2024, approximately eight weeks after plating. Three wells were recorded each for a duration of 1 hour and 48 minutes (120 sec/config) using the MaxTwo 6-well HD-MEA plates from Maxwell Biosystems [28]. The sampling rate of the recording was 10 kHz. The 6 wells on the HD-MEA have a grid of  $220 \times 120$  or 26,400 recording electrodes with 1020 electrodes being accessible at the same time. The electrode center-to-center distance equals 17.5  $\mu\text{m}$ . The active sensing area (ASA) of each well of the MaxTwo 6-well HD-MEA plate is  $3.85 \times 2.10 \text{ mm}^2$  [29], [5]. The raw recording data was spike-sorted using the integrated spike sorting feature of the MaxLab Live Software by MaxWell Biosystems [13]. Of the six recorded wells, three wells had sufficient intrinsic activity for spike-sorting.

### 4.3 Microscope Images and Cell Coloring

We imaged sensory neurons expressing tdTomato on the HD-MEA chip using a Nikon NiE upright confocal microscope equipped with a Yokogawa W1 spinning-disk scan head at 10x magnification. The images were taken after the HD-MEA recording (section 4.2).

## 4.4 Neuronal Conduction Velocity Estimation

Estimating neuronal conduction velocities from HD-MEA recordings involves calculating the velocity of each inferred axonal segment along the paths in the extracted neuronal skeleton (section 4.5.2). From these segment velocities, the total average conduction velocity for each path can be determined, as well as the latency of signal propagation along the entire path.

### 4.4.1 Path Segment Velocity Computation

For each path, the velocity of a segment, defined by two directly connected centroids, was computed using the Euclidean distance between the centroids in pixels, converted to micrometers ( $\mu\text{m}$ ) using a pixel-to-micrometer conversion factor ( $\text{px\_to\_um}$ ). This conversion factor is derived by mapping the pixel dimensions of the GIF ( $908 \times 497$  pixels) to the physical dimensions of the HD-MEA electrode array ( $3.85 \times 2.10 \text{ mm}^2$ ). The time interval for each segment is determined by the difference in the frames in which the centroids were detected, where each frame corresponds to 0.05 ms. The segment velocity ( $v_{\text{segment}}$ ) is calculated as:

$$v_{\text{segment}} = \frac{\text{Distance in Micrometers}}{\text{Frame Difference} \times 0.05 \text{ ms}}$$

This segment velocity captures the conduction speed of the neuronal signal between two directly connected centroids in a path.

### 4.4.2 Total Path Average Velocity Computation

The average velocity for an entire path ( $v_{\text{average}}$ ) is determined by dividing the total path length (sum of segment distances) by the total time taken to traverse the path. The total time is calculated from the difference between the frame of the last centroid and the frame of the first centroid in the path:

$$v_{\text{average}} = \frac{\text{Total Path Length in Micrometers}}{(\text{Frame}_{\text{last}} - \text{Frame}_{\text{first}}) \times 0.05 \text{ ms}}$$

This average velocity captures the average conduction speed of the neuronal signal along the entire path.

### 4.4.3 Path Latency Computation

Latency represents the time delay as the signal travels along the path away from its initiation site. For each centroid  $i$  along the path, the latency ( $\text{Latency}_i$ ) is calculated as the difference between the frame of the current

centroid ( $\text{Frame}_i$ ) and the frame of the first centroid ( $\text{Frame}_{\text{first}}$ ), multiplied by the time per frame (0.05 ms):

$$\text{Latency}_i = (\text{Frame}_i - \text{Frame}_{\text{first}}) \times 0.05 \text{ ms}$$

This latency is computed for each centroid, allowing for the visualization of the temporal progression of neuronal activity along the entire path (Figure 3.7).

## 4.5 Pipeline for Neuronal Analysis

The developed analysis pipeline utilizes spike-sorted data obtained from whole-array axon tracking recordings on high-density microelectrode arrays (HD-MEAs). The spike-sorted data represents the neuronal activity of an individual neuron estimated sequentially across all electrodes of the HD-MEA. Figure 3.13 depicts the spike-triggered extracellular action potential (AP) waveforms, the so-called electrical footprint, for a single neuron recorded across all electrodes. The amplitude of the AP signal is highest near the axon initial segment, and/or the cell soma [25]. In addition to this temporal view, we also depict the spatial distribution of this electrical footprint in Figure 3.12; here the AP waveforms are depicted at their respective electrode positions on the HD-MEA. The integration of this temporal and spatial data will serve as the primary input for the analysis pipeline. The analysis pipeline consists of five modules, which will be discussed in detail in this section.

### 4.5.1 Module 1: Visualization of Neuronal Activity Dynamics Using 3D Matrix Data and GIF Creation

The input for the first analysis pipeline module consists of 3D matrices describing the spatial and temporal dynamics of the electrical footprint for each unit (all data is stored as .npy files). The dimensions of the matrices are  $120 \times 220 \times 65$ , where the x and y axes represent the electrode locations, and the z axis corresponds to time. Each step along the z-axis reflects a time interval of 0.1 ms (sampling rate of 10 kHz), with a total length of 6.5 ms. Thus, each entry in the matrix describes the amplitude recorded by the electrode at location (x, y) at a specific time step z.

To visualize the temporal dynamics of the electrical signals, the matrix data was converted into a GIF. This is done by sequentially processing each slice along the z-axis (which represents different time points). For each time step, a corresponding frame is generated, capturing the spatial distribution of the recorded amplitudes across the electrode array. The amplitude values from the matrix are encoded in the frame using specific colors: orange to bright yellow pixels indicate a range from lower to higher negative voltages,

while light blue to dark blue pixels depict a range from lower to higher positive voltages. Green pixels represent noise or voltages very close to zero. These frames are then compiled into a GIF that dynamically illustrates the progression of neuronal activity over the entire 6.5 ms time window. To enhance temporal resolution, the data along the z-axis is interpolated by a factor of two, meaning each frame in the generated GIF now corresponds to 0.05 ms. This visualization method effectively conveys the dynamic patterns of neuronal activity across the electrode array, with each of the 130 frames displaying a specific time slice at an image resolution of  $908 \times 497$  pixels.

#### **4.5.2 Module 2: Neuronal Footprint Skeletonization and Post-Processing for Accurate Path Reconstruction**

The next module of the analysis pipeline, concerns the "skeletonization" of the electrical footprints. Its only input is a directory containing the GIF file for each unit, which was the output of the first module (section 4.5.1). For the subsequent analysis steps, we discarded GIFs with excessive noise levels. The noise was calculated by converting each frame in the GIF to grayscale and applying a Laplacian filter [30] to detect edges, followed by computing the average variance of the Laplacian filter across all frames. If the average variance exceeded a certain threshold (400), the GIF was discarded. For GIFs that passed the noise filtering step, the skeletonization begins. The first step was to identify regions of interest (ROIs) in each frame of the input GIF. The objective is to identify ROIs in each frame that represent signals from actual neural compartments to correctly infer the neuronal skeleton. Three different approaches were tested:

- 1) Extract the locations of yellow ROIs (Large Negative Amplitudes).
- 2) Extract the locations of blue ROIs (Large Positive Amplitudes).
- 3) Extract the location of both yellow and blue ROIs and fuse them.

The method focusing solely on blue ROIs (negative AP signal peaks) yielded the best results. This is because, in the HSV color spectrum, bright yellows (representing large negative amplitudes) are closer to green (i.e. closer to the noise floor) than dark blue values (representing large positive amplitudes). Although the aim is to extract large negative amplitudes, as they are potential indicators of the depolarization phase in extracellular APs, doing so increased the likelihood of including noise, leading to unwanted path branches. The initial negative peak of an extracellular AP is typically followed by a positive peak during the subsequent repolarization phase, allowing the blue ROIs to accurately form the neuronal skeleton. Using both yellow and blue ROIs decreased accuracy, especially when neuronal processes were close together, as the ROIs then often fused. After applying a mask to detect blue ROIs (lower HSV threshold: [0.55, 0.5, 0.2], higher HSV

threshold: [0.73, 1.0, 1.0]), any ROIs with an area below a minimum size threshold (250 pixels) were discarded to reduce the inclusion of noise in the neuronal skeleton. A second mask, with an increased lower hue value (lower HSV threshold: [0.64, 0.5, 0.2]), was then applied to identify dark blue areas within the larger, lighter blue ROIs detected by the first mask. If no dark blue ROIs are found within a ROI identified by the first mask, the original ROI was retained. If one or more dark blue ROIs larger than a second, smaller minimum size threshold (110 pixels) are found within a ROI detected by the first mask, the ROI detected by the first mask was discarded, and the dark blue ROIs were selected. By applying this approach, we improved the accuracy of tracking splitting points in the neuron, as two dark blue peaks within a larger light blue area can represent two different neuronal processes. For each chosen ROI in the current frame, the centroid was computed.

The next challenge was to establish a connection logic reasonably connecting centroids across consecutive frames. For two centroids to connect, we defined a separation distance of up to 7 frames (0.35 ms). Such a distance was assumed, because there might be cells, such as glial cells, in between the neural compartments and the electrodes on the HD-MEA plate, weakening or completely interrupting the signal. This can lead to discontinuities in the extracted neuronal skeleton if only the previous frame was considered. Another constraint introduces was that the path length between two connected centroids must not exceed a maximum distance threshold. The current threshold (85 pixels or 0.36 mm) allowed for a maximum velocity of 7.2 m/s. The threshold is based on the conduction velocity of C-fibre cells in rats, which were measured and found to be slower than 1.4 m/s [12], [14]. By setting a higher threshold, we introduce a sufficient margin to ensure that the system does not overfit to the slower velocities of C-fibers. Further discussion on the choice of C-fiber conduction velocity can be found in section 3.3.

To select the best centroid connection, we computed a score using a weighted combination of distance and angle. The distance was measured as the Euclidean distance between the two centroids, while the angle was calculated as the offset in degrees from a directional vector based on the last 5 centroids in a path. Both distance and angle were normalized, then multiplied by weighting coefficients of 1 for the distance and 0.8 for the angle. These coefficients were chosen after testing various combinations with up to one decimal place and comparing the visual results. The final score for a possible connection was computed as follows:

$$\text{score} = \text{distance\_coefficient} \times \text{dist\_norm} + \text{angle\_coefficient} \times \text{angle\_norm}$$

After evaluating all possible connections for a centroid in the current frame, the connection with the lowest score was selected. It is important to note that two centroids from one frame can connect to the same centroid from the previous 7 frames, allowing for splits. Once the initial neuronal skeleton was created, post-processing steps were applied to further improve its quality.

In the first step, paths not extending beyond a specified radius (0.3 mm from their starting point) were discarded. This step eliminated many short paths that were created when the AP generated a strong electrical signal that spread to neighboring electrodes as it developed and propagated away from the AIS/soma. This spreading of the AP signal can cause many small blue ROIs (noise) to appear in that region which do not represent actual neuronal structures but still are large enough to form new erroneous paths. Next, path segments between two centroids shorter than 5  $\mu\text{m}$  were discarded, and the resulting gaps were closed. This process was necessary in instances where the signal consistently originated from the same location across several frames, likely from the soma, before it reaches the activation threshold and initiates an AP that propagates away from it. During this period, the detected signal remains localized, but slight variations in the shape of the ROI across frames can cause centroids to be computed very close to each other. These small shifts in centroid positions did not represent meaningful movement of the signal, but rather reflected minor changes in the ROI's contour. Therefore, these short path segments were considered irrelevant for tracing the actual axonal signal trajectory and were removed to maintain a cleaner, more accurate representation of the neuron's activity propagation/spread. The third post-processing step eliminated short offshoots created by noise. If two paths shared more than 92% of their centroids, the shorter path was discarded. The threshold of 92% was chosen based on empirical observations. Additionally, if the difference between the sets of centroids from the shorter and longer paths contained fewer than 4 elements, the shorter path was also discarded. However, these two thresholds (92% and 4) can be further refined in the future depending on the specific objectives of the analysis—whether the focus is on capturing all processes of a neuron or primarily the main ones. Lastly, all paths consisting of fewer than four centroids after the post-processing steps were also discarded.

#### **4.5.3 Module 3: Axon Classification and Output Visualization Following Post-Processing**

After these post-processing steps, axons were classified as detailed in the Results and Discussion chapter (3). Firstly, the split point coordinates of the paths were computed. Then, for each split, the two path sets were computed. Each set contained one of the two main paths that split from each other at that split point. If a path later splits from one of these two main paths, it is added to the set containing that main path. Next, the average velocities of both path sets are calculated, and the velocity difference in percentage is determined. The split point with the largest velocity difference is chosen, and all paths in the slower velocity path set are classified as belonging to the central axon, while those in the faster velocity path set are classified as belonging to the

peripheral axon. If the difference is less than 24%, no classification is made. This classification threshold relies on previously reported differences in conduction velocity between the central and peripheral processes in primary sensory neurons of rats and cats [12], [21].

Examples of all outputs from this module, except for the CSV file and the mask overlay file, are discussed in the Results and Discussion chapter (3). The first output is a CSV file that stores the centroids of each path and their corresponding frame indices, facilitating easy reconstruction of the neuronal skeleton. The second output is a PNG file, displaying the neuronal skeleton with a gradient from blue to gray to red, indicating the latency from the starting point in milliseconds (Figure 3.7). The third output is the input GIF with the neuronal skeleton construction overlaid. In this GIF, the user can visually follow the exact construction of the skeleton before the post-processing steps and assess its quality by comparing it to the original input GIF. The fourth output is another GIF file which displays the chosen ROIs and their centroids in each frame overlaid on the corresponding frame from the input GIF in grayscale. This output is particularly useful for the user to exactly analyze cases where the connection logic was not correct. An example of a frame from this output GIF is shown in Figure 4.1. The fifth output is a PNG which displays a general overview of different metrics for all analyzed neurons (Figure 3.11). Finally, the sixth output is a PNG which displays the post-processed skeleton of the neuron, in which each path has a different color. Next to the post-processed skeleton, there is a graph which shows the velocities along each path. Additionally, there is a legend which indicates for each path; corresponding color, classification, total length, and average velocity. The title points out whether there was a classification of the paths or not and includes the maximum velocity difference across all split points in a neuronal skeleton in percent (Figure 3.14).

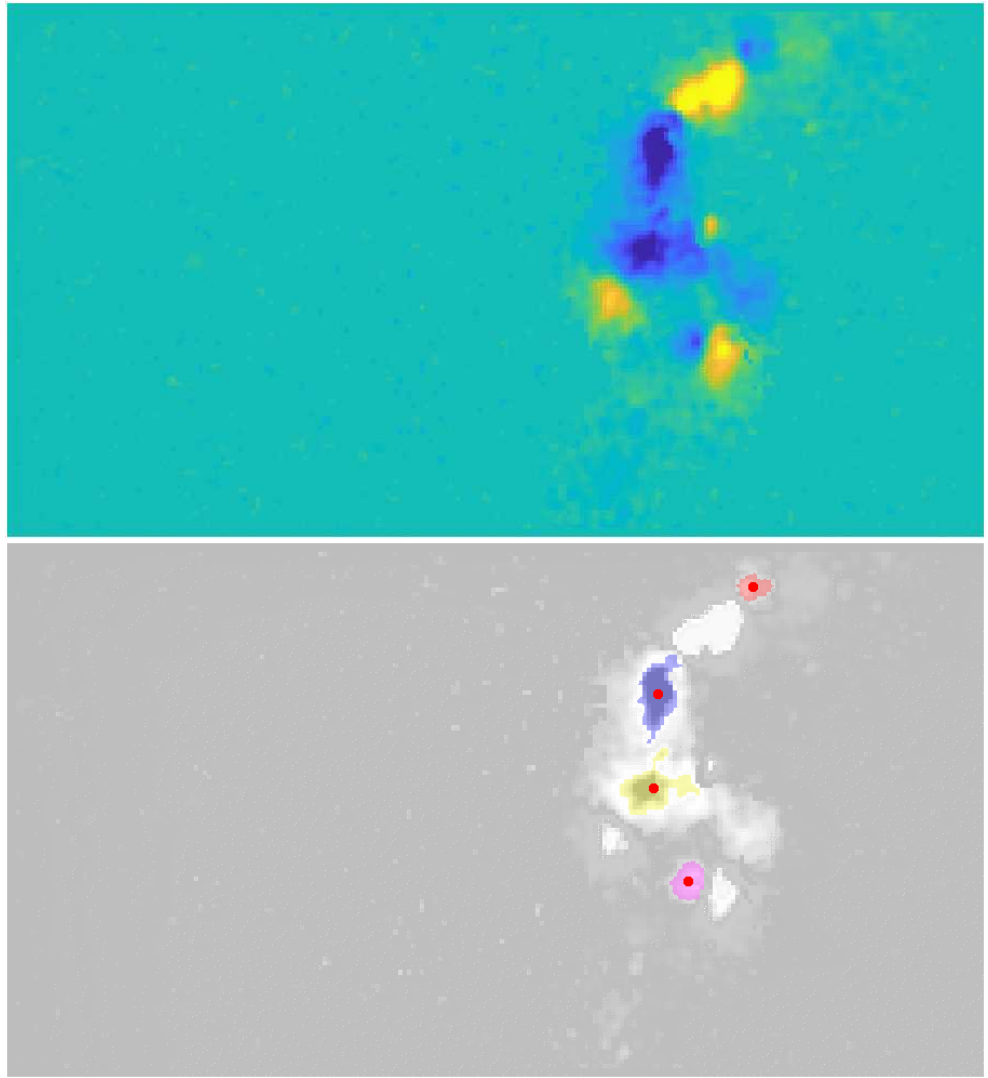


**Figure 4.1:** Frame 19 from the input GIF of unit 21 on well 5. (Bottom) Frame 19 from the mask overlay output GIF generated by the gifskeletonization.py program for unit 21 on well 5.

#### **4.5.4 Module 4: Inferring HD-MEA Electrode Configurations for Targeted Neuronal Stimulation**

The fourth module in the analysis pipeline consists of a program that can be used to infer HD-MEA electrode configurations that can later be used for the targeted electrical stimulation of neurons within the MaxLab Live Software by MaxWell Biosystems [13]. The program's input are the CSV files of each unit, which are outputted by module 3 in the analysis pipeline (section 4.5.2). Because the centroid coordinates in the CSV file are still on the scale of the GIF image size ( $908 \times 497$ ) the program first transforms these coordinates to the scale of the electrode grid ( $120 \times 220$ ) and rounds them to integers. Now, each coordinate corresponds to a specific electrode. Next, we reconstructed the neuronal skeleton using the Bresenham line algorithm [31]. This algorithm was chosen because it efficiently determines which pixels should be selected to form a close approximation to a straight line between two points. This results in a list of electrode coordinates that are part of the reconstructed neuronal skeleton of a neuron. An electrode configuration in the MaxLab Live Software by MaxWell Biosystems [13] consists of 1020 electrodes. Thus, if these 1020 electrodes have already been found after this step, the program outputs these electrode IDs. If the neuronal skeleton is very large, it can also happen that more than 1020 electrodes lie on it. In this case, the program discards the electrodes at the end of the paths that have the longest distance to the initiation site until the desired number (1020) is reached. In most cases the neuronal skeletons were composed of fewer than 1020 electrodes. The remaining electrodes are chosen by calculating the Euclidean distance of each not chosen electrode to the nearest chosen electrode. The points with the shortest distances are added until a total of 1020 electrodes has been reached. The final step is to calculate the electrode IDs from their coordinates. This is necessary to use the electrode configuration in the MaxLab Live Software by MaxWell Biosystems [13]. The electrode IDs can be calculated with the following formula:  $ID = x \times (\text{number of columns (220)}) + y + 1$ . The chosen electrode IDs for each unit are then saved as an increasing sorted list in a .json file. Additionally, we generated a PNG image, which visualizes the final set of electrodes in red (all remaining electrodes are depicted in blue). This enables the user to easily check the correctness of the selection. An example is shown in Figure 4.2.

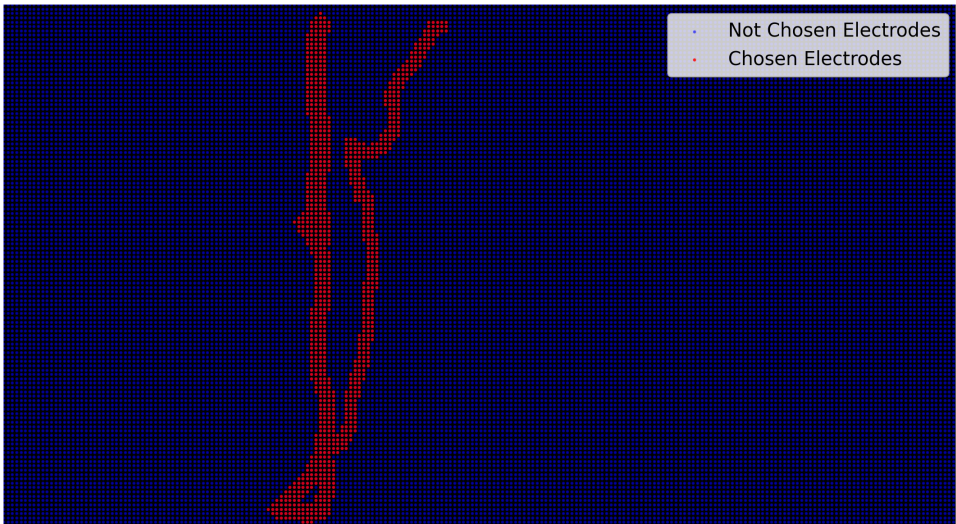


**Figure 4.2:** Visualised electrode configuration computed by the extract-electrodes.py program for unit 22 from well 1. The chosen electrodes for the recording configuration are displayed in red and the not chosen electrodes in blue. The extracted final neuronal skeleton can be found in Figure 3.3.

#### 4.5.5 Module 5: Amplitude Waveform Visualization of Neuronal Activity Along Reconstructed Paths

To effectively analyze and interpret neural activity, it is crucial to visualize how the measured signals evolve over time and across different neuronal compartments. The amplitudes.py program provides a detailed visualization of neural activity by overlaying amplitude data on the neuronal skeletons paths. The generated plots allow for an in-depth analysis of the temporal and spatial dynamics of neural activity along the paths. An example of this output is shown in Figure 3.12. The program specifically visualizes the average measured amplitude over a 6.5 ms time window for selected electrodes located on the neuronal skeleton. It processes input .npy files, containing raw amplitude data, and .CSV files, containing path data. The .npy files are interpolated along the time axis using linear interpolation by a factor of two. This interpolation is necessary to match the temporal resolution used in the GIF creation process in the AxonTracking.m program. To accurately align the path coordinates with the electrode data, the centroid coordinates from the .CSV file are translated and scaled to fit within a  $120 \times 220$  grid, corresponding to the spatial resolution of the electrode array. For each time point, the average amplitude is computed over  $4 \times 4$  blocks of electrodes. The resulting average amplitudes are then connected across all 130 (0.05 ms) time steps, resulting in an amplitude-over-time (waveform) plot, spanning the entire 6.5 ms time window. The program evaluates each

waveform plot to determine if its largest positive or negative peak exceeds the respective user-defined thresholds in microvolts. Waveforms plots with a threshold-exceeding peak are included in the amplitude visualization with a color-coded representation to indicate the maximum trough value. A color bar is included to map the colors to their corresponding amplitude values (pink: small negative amplitudes, light blue large negative amplitudes).

# Outlook

---

The analysis pipeline presents many opportunities for enhancement, starting with simple things such as changing the HSV color mapping in the Axon-ScanTest.m program to better isolate large negative amplitudes from noise. Fine-tuning the parameters within the code, for example, the maximum connection length for linking centroids, could be achieved using more sophisticated automated techniques. Moreover, determining an optimal spike sorting framework remains essential to accurately capture the electrical footprints of individual neurons.

To date, the analysis pipeline has only implemented a very limited analysis of the waveforms within the electrical footprints of neurons. Incorporating a detailed waveform analysis could further refine the accuracy of the extracted neuronal skeletons. Post-processing the final neuronal skeletons by comparing them to their corresponding electrical footprints could make it possible to correct misaligned segments to improve the precision of the final neuronal skeleton. Moreover, implementing an automated analysis of waveform shape and how it changes along the neuronal skeleton could enable an improved detection and classification of neuronal compartments and their functionalities. Preprocessing techniques that exclude neurons lacking their initiation site or soma on the MEA plate could simplify morphological classification. Leveraging the inferred electrode configurations (section 4.5.4), to perform more detailed analyses of neuronal behavior using the stimulation functionality in MaxLab Live Software [13] could yield additional insights into the conduction properties of neurons *in vitro*. Moreover, identifying regions on the neuron that are most effective for inducing action potentials via controlled stimulation has been a focal point of research in recent years [32], [33]. Furthermore, an iterative approach—where the electrode configuration is used to perform a subsequent, more precise recording, using only electrodes proximal to the neuron—could lead to more accurate electrical footprints, thereby enhancing the quality of the neuronal skeleton.

Finally, integrating machine learning techniques, as recently demonstrated by Hornauer et al. [24], could significantly enhance the electrophysiological phenotyping of neurons. By integrating unsupervised learning methods or supervised approaches when more ground truths are available, the pipeline could be advanced to provide more accurate and automated phenotyping. Simulated data, as utilized by Buccino et al. [6] to provide ground truths, offers another promising avenue for model training. However, ensuring the robustness of such models in the face of the complex, real-world behavior of neural networks remains a significant challenge.

By considering these enhancements, the analysis pipeline could evolve into a powerful tool for comprehensive neuronal analysis, offering significant contributions to the field of neuroscience.

---

## Bibliography

---

- [1] C. J. LeBlang *et al.*, "Satellite glial contact enhances differentiation and maturation of human induced sensory neurons," *bioRxiv*, 2024. doi: [10.1101/2024.07.24.604966](https://doi.org/10.1101/2024.07.24.604966). [Online]. Available: <https://www.biorxiv.org/content/early/2024/07/24/2024.07.24.604966>.
- [2] Y. Umehara *et al.*, "Robust induction of neural crest cells to derive peripheral sensory neurons from human induced pluripotent stem cells," *Scientific Reports*, vol. 10, no. 1, p. 4360, Mar. 2020, issn: 2045-2322. doi: [10.1038/s41598-020-60036-z](https://doi.org/10.1038/s41598-020-60036-z). [Online]. Available: <https://doi.org/10.1038/s41598-020-60036-z>.
- [3] P.-H. T. Temugin Berta Yawar Qadri and R.-R. Ji, "Targeting dorsal root ganglia and primary sensory neurons for the treatment of chronic pain," *Expert Opinion on Therapeutic Targets*, vol. 21, no. 7, pp. 695–703, 2017, PMID: 28480765. doi: [10.1080/14728222.2017.1328057](https://doi.org/10.1080/14728222.2017.1328057). eprint: <https://doi.org/10.1080/14728222.2017.1328057>. [Online]. Available: <https://doi.org/10.1080/14728222.2017.1328057>.
- [4] M. E. J. Obien, K. Deligkaris, T. Bullmann, D. J. Bakkum, and U. Frey, "Revealing neuronal function through microelectrode array recordings," *Frontiers in Neuroscience*, vol. 8, 2015, issn: 1662-453X. doi: [10.3389/fnins.2014.00423](https://doi.org/10.3389/fnins.2014.00423). [Online]. Available: <https://www.frontiersin.org/journals/neuroscience/articles/10.3389/fnins.2014.00423>.
- [5] J. Müller *et al.*, "High-resolution cmos mea platform to study neurons at subcellular, cellular, and network levels," *Lab Chip*, vol. 15, pp. 2767–2780, 13 2015. doi: [10.1039/C5LC00133A](https://doi.org/10.1039/C5LC00133A). [Online]. Available: <http://dx.doi.org/10.1039/C5LC00133A>.
- [6] A. P. Buccino, X. Yuan, V. Emmenegger, X. Xue, T. Gänswein, and A. Hierlemann, "An automated method for precise axon reconstruction from recordings of high-density micro-electrode arrays," *Journal of Neural Engineering*, vol. 19, no. 2, p. 026026, Mar. 2022. doi: [10.1088/1741-2552/ac59a2](https://doi.org/10.1088/1741-2552/ac59a2). [Online]. Available: <https://doi.org/10.1088/1741-2552/ac59a2>.
- [7] M. Radivojevic and A. Rostedt Punga, "Functional imaging of conduction dynamics in cortical and spinal axons," *eLife*, vol. 12, M. Radisic, P. Poirazi, and M. Radisic, Eds., e86512, Aug. 2023, issn: 2050-084X. doi: [10.7554/eLife.86512](https://doi.org/10.7554/eLife.86512). [Online]. Available: <https://doi.org/10.7554/eLife.86512>.

- [8] S. Ronchi *et al.*, "Electrophysiological phenotype characterization of human ipsc-derived neuronal cell lines by means of high-density microelectrode arrays," *Advanced Biology*, vol. 5, no. 3, pp. 200–223, 2021. doi: <https://doi.org/10.1002/adbi.202000223>. eprint: <https://onlinelibrary.wiley.com/doi/pdf/10.1002/adbi.202000223>. [Online]. Available: <https://onlinelibrary.wiley.com/doi/abs/10.1002/adbi.202000223>.
- [9] R. Guarnieri, "Real-time analysis of high-density eeg signals for closed-loop applications," Ph.D. dissertation, KU Leuven, Groep Biomedische Wetenschappen, Faculteit Bewegings- en Revalidatiewetenschappen, Departement Bewegingswetenschappen, May 2021. [Online]. Available: [https://www.researchgate.net/publication/352296761\\_Real-time\\_analysis\\_of\\_high-density\\_EEG\\_signals\\_for\\_closed-loop\\_applications](https://www.researchgate.net/publication/352296761_Real-time_analysis_of_high-density_EEG_signals_for_closed-loop_applications).
- [10] A. I. Nascimento, F. M. Mar, and M. M. Sousa, "The intriguing nature of dorsal root ganglion neurons: Linking structure with polarity and function," *Progress in Neurobiology*, vol. 168, pp. 86–103, 2018, ISSN: 0301-0082. doi: <https://doi.org/10.1016/j.pneurobio.2018.05.002>. [Online]. Available: <https://www.sciencedirect.com/science/article/pii/S0301008217302101>.
- [11] J. Moini, A. LoGalbo, and R. Ahangari, "Chapter 3 - neural tissue," in *Foundations of the Mind, Brain, and Behavioral Relationships*, J. Moini, A. LoGalbo, and R. Ahangari, Eds., Academic Press, 2024, pp. 39–62, ISBN: 978-0-323-95975-9. doi: <https://doi.org/10.1016/B978-0-323-95975-9.00017-2>. [Online]. Available: <https://www.sciencedirect.com/science/article/pii/B9780323959759000172>.
- [12] P. J. e. a. Waddell, "Conduction velocity changes along the processes of rat primary sensory neurons," *Neuroscience*, pp. 577–84, 1989. doi: [doi:10.1016/0306-4522\(89\)90152-8](https://doi.org/10.1016/0306-4522(89)90152-8).
- [13] M. B. AG, *Maxlab live software*, Accessed: 2024-07-31, 2024. [Online]. Available: <https://www.mxwbiao.com/products/maxlab-live-software/>.
- [14] A. A. Harper and S. N. Lawson, "Conduction velocity is related to morphological cell type in rat dorsal root ganglion neurones," *The Journal of Physiology*, vol. 359, pp. 31–46, 1 1985. doi: [10.1113/jphysiol.1985.sp015573](https://doi.org/10.1113/jphysiol.1985.sp015573).
- [15] V. Villière and E. M. McLachlan, "Electrophysiological properties of neurons in intact rat dorsal root ganglia classified by conduction velocity and action potential duration," en, *J Neurophysiol*, vol. 76, no. 3, pp. 1924–1941, Sep. 1996.

- [16] A. R. Costa, R. Pinto-Costa, S. C. Sousa, and M. M. Sousa, "The regulation of axon diameter: From axonal circumferential contractility to activity-dependent axon swelling," *Frontiers in Molecular Neuroscience*, vol. 11, 2018, ISSN: 1662-5099. doi: [10.3389/fnmol.2018.00319](https://doi.org/10.3389/fnmol.2018.00319). [Online]. Available: <https://www.frontiersin.org/journals/molecular-neuroscience/articles/10.3389/fnmol.2018.00319>.
- [17] G. Matsumoto and I. Tasaki, "A study of conduction velocity in non-myelinated nerve fibers," *Biophysical Journal*, vol. 20, no. 1, pp. 1–13, 1977, ISSN: 0006-3495. doi: [https://doi.org/10.1016/S0006-3495\(77\)85532-X](https://doi.org/10.1016/S0006-3495(77)85532-X). [Online]. Available: <https://www.sciencedirect.com/science/article/pii/S000634957785532X>.
- [18] S. Matsuda *et al.*, "Morphological transformation of sensory ganglion neurons and satellite cells," *Biomedical Reviews*, vol. 11, p. 39, Mar. 2000. doi: [10.14748/bmr.v11.129](https://doi.org/10.14748/bmr.v11.129).
- [19] A. I. Nascimento *et al.*, "Sensory neurons have an axon initial segment that initiates spontaneous activity in neuropathic pain," *Brain*, vol. 145, no. 5, pp. 1632–1640, May 2022, ISSN: 0006-8950. doi: [10.1093/brain/awac078](https://doi.org/10.1093/brain/awac078). eprint: <https://academic.oup.com/brain/article-pdf/145/5/1632/43948491/awac078.pdf>. [Online]. Available: <https://doi.org/10.1093/brain/awac078>.
- [20] J. Mateus *et al.*, "Neuronal cultures show bidirectional axonal conduction with antidromic action potentials depolarizing the soma," *bioRxiv*, 2021. doi: [10.1101/2021.03.07.434278](https://doi.org/10.1101/2021.03.07.434278). eprint: <https://www.biorxiv.org/content/early/2021/06/22/2021.03.07.434278.full.pdf>. [Online]. Available: <https://www.biorxiv.org/content/early/2021/06/22/2021.03.07.434278>.
- [21] G. Czéh, N. Kudo, and M. Kuno, "Membrane properties and conduction velocity in sensory neurones following central or peripheral axotomy," *The Journal of Physiology*, vol. 270, no. 1, pp. 165–180, 1977. doi: <https://doi.org/10.1113/jphysiol.1977.sp011944>. eprint: <https://physoc.onlinelibrary.wiley.com/doi/pdf/10.1113/jphysiol.1977.sp011944>. [Online]. Available: <https://physoc.onlinelibrary.wiley.com/doi/abs/10.1113/jphysiol.1977.sp011944>.
- [22] J. A. Assad *et al.*, "Brain function: Novel technologies driving novel understanding," in *Bioinspired Approaches for Human-Centric Technologies*, R. Cingolani, Ed. Cham: Springer International Publishing, 2014, pp. 299–334, ISBN: 978-3-319-04924-3. doi: [10.1007/978-3-319-04924-3\\_10](https://doi.org/10.1007/978-3-319-04924-3_10). [Online]. Available: [https://doi.org/10.1007/978-3-319-04924-3\\_10](https://doi.org/10.1007/978-3-319-04924-3_10).

- [23] D. Contreras, "Electrophysiological classes of neocortical neurons," *Neural Networks*, vol. 17, no. 5, pp. 633–646, 2004, Vision and Brain, ISSN: 0893-6080. doi: <https://doi.org/10.1016/j.neunet.2004.04.003>. [Online]. Available: <https://www.sciencedirect.com/science/article/pii/S0893608004000863>.
- [24] P. Hornauer *et al.*, "Deepphys: A machine learning–assisted platform for electrophysiological phenotyping of human neuronal networks," *STEM CELL REPORTS*, vol. 19, pp. 285–298, 2 2024. doi: <10.1016/j.stemcr.2023.12.008>. [Online]. Available: <https://doi.org/10.1016/j.stemcr.2023.12.008>.
- [25] D. J. Bakkum *et al.*, "The axon initial segment is the dominant contributor to the neuron's extracellular electrical potential landscape," *Advanced Biosystems*, vol. 3, no. 2, p. 1800308, 2019. doi: <https://doi.org/10.1002/adbi.201800308>. eprint: <https://onlinelibrary.wiley.com/doi/pdf/10.1002/adbi.201800308>. [Online]. Available: <https://onlinelibrary.wiley.com/doi/abs/10.1002/adbi.201800308>.
- [26] M. Schröter *et al.*, "Functional imaging of brain organoids using high-density microelectrode arrays," *MRS Bulletin*, vol. 47, no. 6, pp. 530–544, Jun. 2022, ISSN: 1938-1425. doi: <10.1557/s43577-022-00282-w>. [Online]. Available: <https://doi.org/10.1557/s43577-022-00282-w>.
- [27] S. Someck, A. Levi, H. E. Sloin, L. Spivak, R. Gattegno, and E. Stark, "Positive and biphasic extracellular waveforms correspond to return currents and axonal spikes," *Communications Biology*, vol. 6, no. 1, p. 950, Sep. 2023, ISSN: 2399-3642. doi: <10.1038/s42003-023-05328-6>. [Online]. Available: <https://doi.org/10.1038/s42003-023-05328-6>.
- [28] M. B. AG, *Maxtwo well plates*, Accessed: 2024-08-09, 2024. [Online]. Available: <https://www.mxwbio.com/maxtwo-well-plates/>.
- [29] M. Ballini *et al.*, "A 1024-channel cmos microelectrode array with 26,400 electrodes for recording and stimulation of electrogenic cells in vitro," *IEEE Journal of Solid-State Circuits*, vol. 49, no. 11, pp. 2705–2719, 2014. doi: <10.1109/JSSC.2014.2359219>.
- [30] O. Team, *Opencv: Open source computer vision library*, Version 4.10.0, 2024. [Online]. Available: [https://docs.opencv.org/4.x/d5/db5/tutorial\\_laplace\\_operator.html](https://docs.opencv.org/4.x/d5/db5/tutorial_laplace_operator.html).
- [31] J. E. Bresenham, "Algorithm for computer control of a digital plotter," *IBM Systems Journal*, vol. 4, no. 1, pp. 25–30, 1965.

- [32] M. Radivojevic, D. Jäckel, and M. e. a. Altermatt, "Electrical identification and selective microstimulation of neuronal compartments based on features of extracellular action potentials," *scientific reports*, vol. 12, p. 31 332, Aug. 2016. doi: <https://doi.org/10.1038/srep31332>. [Online]. Available: <https://doi.org/10.1038/srep31332>.
- [33] S. Ronchi *et al.*, "Single-cell electrical stimulation using cmos-based high-density microelectrode arrays," *Frontiers in Neuroscience*, vol. 13, 2019, issn: 1662-453X. doi: <10.3389/fnins.2019.00208>. [Online]. Available: <https://www.frontiersin.org/journals/neuroscience/articles/10.3389/fnins.2019.00208>.
- [34] L. Kanari *et al.*, "Computational synthesis of cortical dendritic morphologies," *Cell Reports*, vol. 39, no. 1, p. 110 586, 2022, issn: 2211-1247. doi: <https://doi.org/10.1016/j.celrep.2022.110586>. [Online]. Available: <https://www.sciencedirect.com/science/article/pii/S2211124722003308>.
- [35] L. Kanari *et al.*, "Objective Morphological Classification of Neocortical Pyramidal Cells," *Cerebral Cortex*, vol. 29, no. 4, pp. 1719–1735, Jan. 2019, issn: 1047-3211. doi: <10.1093/cercor/bhy339>. eprint: <https://academic.oup.com/cercor/article-pdf/29/4/1719/28075646/bhy339.pdf>. [Online]. Available: <https://doi.org/10.1093/cercor/bhy339>.
- [36] A. Mudge, "Schwann cells induce morphological transformation of sensory neurones in vitro," *Nature*, vol. 309, no. 5966, pp. 367–369, 1984, issn: 0028-0836. doi: <10.1038/309367a0>. [Online]. Available: <https://doi.org/10.1038/309367a0>.
- [37] S. Meltzer, C. Santiago, N. Sharma, and D. D. Ginty, "The cellular and molecular basis of somatosensory neuron development," *Neuron*, vol. 109, no. 23, pp. 3736–3757, 2021, issn: 0896-6273. doi: <https://doi.org/10.1016/j.neuron.2021.09.004>. [Online]. Available: <https://www.sciencedirect.com/science/article/pii/S0896627321006589>.
- [38] Queensland Brain Institute. "Types of neurons." Image credit: iStockphoto. (2024), [Online]. Available: <https://qbi.uq.edu.au/brain/brain-anatomy/types-neurons>.
- [39] C. M. Muzio MR, "Histology, axon," in *StatPearls*, R. Cingolani, Ed. StatPearls Publishing, 2022. [Online]. Available: <https://www.ncbi.nlm.nih.gov/books/NBK554388/>.
- [40] A. A. Robbins, S. E. Fox, G. L. Holmes, R. C. Scott, and J. M. Barry, "Short duration waveforms recorded extracellularly from freely moving rats are representative of axonal activity," *Frontiers in Neural Circuits*,

- vol. 7, 2013, ISSN: 1662-5110. doi: [10.3389/fncir.2013.00181](https://doi.org/10.3389/fncir.2013.00181). [Online]. Available: <https://www.frontiersin.org/journals/neural-circuits/articles/10.3389/fncir.2013.00181>.
- [41] K. R. Tovar *et al.*, “Action potential propagation recorded from single axonal arbors using multielectrode arrays,” *Journal of Neurophysiology*, vol. 120, no. 1, pp. 306–320, 2018, PMID: 29641308. doi: [10.1152/jn.00659.2017](https://doi.org/10.1152/jn.00659.2017). eprint: <https://doi.org/10.1152/jn.00659.2017>. [Online]. Available: <https://doi.org/10.1152/jn.00659.2017>.
  - [42] X. Jia *et al.*, “High-density extracellular probes reveal dendritic back-propagation and facilitate neuron classification,” *Journal of Neurophysiology*, vol. 121, no. 5, pp. 1831–1847, 2019, PMID: 30840526. doi: [10.1152/jn.00680.2018](https://doi.org/10.1152/jn.00680.2018). eprint: <https://doi.org/10.1152/jn.00680.2018>. [Online]. Available: <https://doi.org/10.1152/jn.00680.2018>.
  - [43] C. Gold, D. A. Henze, C. Koch, and G. Buzsáki, “On the origin of the extracellular action potential waveform: A modeling study,” *Journal of Neurophysiology*, vol. 95, no. 5, pp. 3113–3128, 2006, PMID: 16467426. doi: [10.1152/jn.00979.2005](https://doi.org/10.1152/jn.00979.2005). eprint: <https://doi.org/10.1152/jn.00979.2005>. [Online]. Available: <https://doi.org/10.1152/jn.00979.2005>.

**Declaration of originality**

The signed declaration of originality is a component of every written paper or thesis authored during the course of studies. In consultation with the supervisor, one of the following three options must be selected:

- I confirm that I authored the work in question independently and in my own words, i.e. that no one helped me to author it. Suggestions from the supervisor regarding language and content are excepted. I used no generative artificial intelligence technologies<sup>1</sup>.
- I confirm that I authored the work in question independently and in my own words, i.e. that no one helped me to author it. Suggestions from the supervisor regarding language and content are excepted. I used and cited generative artificial intelligence technologies<sup>2</sup>.
- I confirm that I authored the work in question independently and in my own words, i.e. that no one helped me to author it. Suggestions from the supervisor regarding language and content are excepted. I used generative artificial intelligence technologies<sup>3</sup>. In consultation with the supervisor, I did not cite them.

**Title of paper or thesis:**

Characterization of Human iPSC-Derived Sensory Neuron Morphology on HD-MEAs

**Authored by:**

*If the work was compiled in a group, the names of all authors are required.*

**Last name(s):**

Stüger

**First name(s):**

Martin Alexander

With my signature I confirm the following:

- I have adhered to the rules set out in the Citation Guide.
- I have documented all methods, data and processes truthfully and fully.
- I have mentioned all persons who were significant facilitators of the work.

I am aware that the work may be screened electronically for originality.

**Place, date**

Zürich, 28.08.2024

**Signature(s)**



*If the work was compiled in a group, the names of all authors are required. Through their signatures they vouch jointly for the entire content of the written work.*

<sup>1</sup> E.g. ChatGPT, DALL E 2, Google Bard

<sup>2</sup> E.g. ChatGPT, DALL E 2, Google Bard

<sup>3</sup> E.g. ChatGPT, DALL E 2, Google Bard